Biochemical Pharmacology 243 (2026) 117448

Contents lists available at ScienceDirect

Biochemical Pharmacology

journal homepage: www.elsevier.com/locate/biochempharm

Toward the development of an innovative pharmacological compound employing peptides for EGFR-mediated drug delivery in anaplastic thyroid carcinoma

Zehra-Cagla Kahvecioglu [a], Samuel Vandecasteele [a], Marine Bougard [a], Olivia Rasson [a], Amandine Nachtergael [b], Pierre Duez [b], Denis Nonclercq [c], Myriam Remmelink [d], Sophie Laurent [a,e], Sven Saussez [f], Carmen Burtea [a,*]

[a] Unit of General, Organic and Biomedical Chemistry, NMR and Molecular Imaging Laboratory, Faculty of Medicine, Pharmacy and Biomedical Sciences, University of Mons, Avenue Victor Maistriau 19, Mendeleyev building, B-7000 Mons, Belgium
[b] Unit of Therapeutic Chemistry and Pharmacognosy, Faculty of Medicine, Pharmacy and Biomedical Sciences, University of Mons, Chemin du Champ de Mars 25, B-7000 Mons, Belgium
[c] Unit of Histology, Faculty of Medicine, Pharmacy and Biomedical Sciences, University of Mons, Pentagon building, Avenue du Champ de Mars 6, Pentagone building, B-7000 Mons, Belgium
[d] Department of Pathological Anatomy, Erasme Hospital, Faculty of Medicine, Campus Erasme, CP 556, Route de Lennik, 808 1070 Bruxelles, Belgium
[e] Center for Microscopy and Molecular Imaging (CMMI), rue Adrienne Bolland 8, B-6041 Gosselies, Belgium
[f] Human Anatomy and Experimental Oncology Unit, Faculty of Medicine, Pharmacy and Biomedical Sciences, University of Mons, Pentagon building, Avenue du Champ de Mars 6, B-7000 Mons, Belgium

ARTICLE INFO

Keywords:
EGFR
Anaplastic thyroid carcinoma
Targeted delivery
Peptides
Endocytosis

ABSTRACT

Anaplastic thyroid cancer (ATC) represents the deadliest thyroid tumor in humans. Current treatments have not really demonstrated a long-term benefit. Accordingly, targeted drug delivery should be considered to improve the prognosis of patients, but also the early-stage diagnosis. Epidermal Growth Factor Receptor (EGFR) is commonly studied in oncology as it is overexpressed in cancer cells and is actively investigated in the framework of receptor-mediated drug delivery due to its intracellular trafficking. Therefore, an EGFR-targeted peptide was developed in the present work by taking advantage of the versatility of phage display technique.

The selected EGFR-targeted P20 peptide was investigated by a wide range of *in silico*, *in vitro*, *in vivo* and *ex vivo* methods, allowing us to formulate the following main conclusions: (1) P20 has a theoretical half-life of 100 h and binds to EGFR domains that harbor the EGF binding site; (1) the peptide binds in a higher level to cancer cells and tissues compared to healthy ones; (2) it induces EGFR endocytosis and follows the non-degradative EGFR intracellular pathway; (3) P20 does not interfere with EGF binding and acts as a non-competitive inhibitor of EGFR; (4) it could contribute to the therapeutic effect of anti-cancer drugs by decreasing the expression and activation of EGFR, as well as of AKT phosphorylation in ATC cells; (5) P20 does not induce *in vivo* toxic effects in the main tissues and organs; (6) it is concentrated in tumors, where the peptide is retained for longer time than in other tissues due to its binding to EGFR.

Abbreviations: 7-AAD, 7-Aminoactinomycin D; AA%, amino acid composition expressed as a percentage; ABC, Avidin/Biotinylated enzyme Complex; ABTS, 2,2′-azino-bis-3-ethylbenzothioazoline-6-sulfonic acid; A.I., aliphatic index; AKT, protein kinase B; ALT, alanine aminotransferase; AST, aspartate aminotransferase; ATC, anaplastic thyroid carcinoma; Bad, the Bcl2 associated agonist of cell death protein; BCA, Pierce BiCinchoninic Acid; BUN, Blood Urea Nitrogen; CMMI, Center for Microscopy and Molecular Imaging; DAB, 3,3′-diaminobenzidine tetrahydrochloride solution; DAPI, 4′,6-diamidino-2-phenylindole; DTT, dithiothreitol; ECACC, European Collection of Authenticated Cell Cultures; ECL, Enhanced chemiluminescence; ED, extracellular domain; ED-EGFR, Extracellular domain of EGFR; EGF, epidermal growth factor; EGFR, the epidermal growth

* Corresponding author.
E-mail addresses: Zehracagla.KAHVECIOGLU@umons.ac.be (Z.-C. Kahvecioglu), samuel.vandecasteele@police.belgium.eu (S. Vandecasteele), Marine.Bougard@alumni.umons.ac.be (M. Bougard), Olivia.Rasson@umons.ac.be (O. Rasson), Amandine.NACHTERGAEL@umons.ac.be (A. Nachtergael), Pierre.DUEZ@umons.ac.be (P. Duez), Denis.NONCLERCQ@umons.ac.be (D. Nonclercq), Myriam.Remmelink@hubruxelles.be (M. Remmelink), Sophie.LAURENT@umons.ac.be (S. Laurent), Sven.SAUSSEZ@umosn.ac.be (S. Saussez), Carmen.BURTEA@umons.ac.be (C. Burtea).

https://doi.org/10.1016/j.bcp.2025.117448
Received 10 June 2025; Received in revised form 17 August 2025; Accepted 17 October 2025
Available online 21 October 2025

factor receptor; ER, endoplasmic reticulum; FLI, Fluorescence Lifetime Imaging; GAPDH, the glyceraldehyde-3-phosphate dehydrogenase; IC_{50}, the half-maximal inhibitory concentration; IF, immunofluorescence, IHC, immunohistochemistry; IL7R, interleukin 7 receptor; K^*_d, the apparent dissociation constant; LDS, lithium dodecyl sulfate sample buffer; MAPK, Mitogen-Activated Protein Kinase; mTOR, mammalian target of rapamycin; NA: not available; NMRI, The Naval Medical Research Institute (mouse model); NSP: non-stimulated cells incubated with P20-rhodamine; NSPE: non-stimulated cells incubated with P20-rhodamine and soluble EGFR; PAM, the PI3K/AKT/mTOR signaling pathway; PEG, polyethylene glycol; peptide-TR: peptide-Texas Red; PFBB, Protein-Free Blocking Buffer; PI3K, Phosphoinositide 3-kinase; PLCγ/PKC, phospholipase Cγ/protein kinase C; PMSF, phenylmethylsulphonyl fluoride; PS, phosphatidylserine; SP: cells stimulated with EGF and incubated with P20-rhodamine; SPE: cells stimulated with EGF and incubated with P20-rhodamine and soluble EGFR; RET, Rearranged during transfection; RRFL, Relative Ratio of Fluorescent Labeling; RRIL, Relative Ratio of IHC Labeling; RTK, receptor tyrosine kinases; SD: standard deviation; SDS: Sodium Dodecyl Sulfate; SI: signal intensity; T-Bil: total bilirubin; TC, thyroid carcinoma; T-Chol, Total cholesterol; TGF-α, Transforming growth factor alpha; TK, tyrosine kinase; TMB, 3,3′,5,5′-Tetramethylbenzidine; VEGFR, Vascular Endothelial Growth Factor Receptor.

1. Introduction

Epidermal growth factor receptor (EGFR) is a 170 kDa transmembrane protein commonly studied in oncology. It belongs to a family of receptor tyrosine kinases (RTK) that includes four members, namely EGFR/ErbB-1/HER1, ErbB-2/HER2, ErbB-3/HER3, and ErbB-4/HER4 [1]. Human EGFR is composed of a hydrophobic transmembrane domain separating an extracellular region from an intracellular region. The intracellular region is mainly composed of a TK domain preceding a carboxy-terminal tail on which tyrosine autophosphorylation sites are found. The extracellular region comprises the binding domains of EGFR ligands that are growth factors belonging to the EGF family. These can be classified into two classes, namely those that are specific to EGFR such as EGF, TGF-α and amphiregulin, and those that are specific to both EGFR and ErbB4 such as betacellulin, heparin-binding EGF-like growth factor and epiregulin [2]. EGF is the main ligand of EGFR, and it interacts hydrophobically with three EGFR sites, i.e., loop A of EGF interacts with site 2 of L2 domain of EGFR, loop B of EGF interacts with site 1 of L1 domain of EGFR, and C-terminal region of EGF interacts with site 3 of L2 domain of EGFR [3].

The ligand binding results in a conformational change of EGFR, which prompts its dimerization and *trans*-autophosphorylation of Tyr residues located on the cytoplasmic tail. These phosphorylated Tyr residues recruit various intracellular proteins enabling the triggering of several intracellular signaling pathways, promoting cell proliferation, motility, and survival, such as phosphoinositide 3-kinase (PI3K)/AKT/mammalian target of rapamycin (mTOR) (PAM), Mitogen-Activated Protein Kinase (MAPK) and phospholipase Cγ/protein kinase C (PLCγ/PKC) [4,5].

Ligand binding to EGFR induces its endocytosis and the end of the signaling pathway. The receptor travels to early endosomes, from which it can either be recycled to the cell membrane (leading to signal prolongation), degraded in lysosomes (leading to signal attenuation), or sent to another cell compartment [6–9]. EGFR intracellular destinations include the nucleus for transcriptional regulation, mitochondria to increase resistance to apoptosis, and retrograde transport to the endoplasmic reticulum (ER), pathways that were largely investigated in cancer cells [6,7,10,11]. Because of its roles in cell proliferation and resistance to therapies, the presence of nuclear EGFR indicates an advanced stage of cancer and therefore a poor prognosis in patients [7,8,12,13]. Given EGFR involvement in cell growth pathways, its overactivation (increased expression of ligands) or overexpression (gene amplification, increased transcription, decreased degradation) promotes cancer development. Cancers presenting a change in EGFR behavior are aggressive, have rapid growth, drug resistance, and form metastases more frequently [7,14–18].

Therefore, EGFR is often targeted by many cancer-specific molecular therapies, which are either used to block its activation, or the receptor itself is employed to drive agents into cancer cells due to its capacity to be endocytosed. Indeed, nanoparticles such as immunoliposomes and micelles are quite interesting because they can incorporate a certain amount of anti-tumor agents, and their surface can be functionalized by adding EGFR-targeted ligands. EGFR also shows promise in radionuclide therapy, being able to transport these agents bound to an EGFR-targeted molecule within the nucleus of cancer cells [7].

Among endocrine cancers, thyroid carcinoma (TC) is the most common and accounts for 1–3 % of all cancer cases diagnosed each year worldwide [19,20]. TC predominantly affects women, suggesting that hormonal factors may play a role [21]. Undifferentiated TC are more aggressive and generally have a poor prognosis with a median survival of 5 years for poorly differentiated TC and 4 months for anaplastic TC (ATC) after diagnosis. Death is caused by airway obstruction and metastases that occur, in 75 % of ATC cases, in the lungs (80 %), brain (5–13 %) and bones (6–15 %) [22,23]. The ineffectiveness of conventional treatments in improving patient prognosis explains the current development of targeted therapies, which are meant to inhibit either the MAPK or the PAM pathway, both of which being overactivated in TC. Membrane receptors (EGFR, rearranged during transfection (RET), Vascular Endothelial Growth Factor Receptor (VEGFR)) are the primary targets of these pharmacological inhibitors. However, despite current advances in targeted therapies, these therapeutic agents alone do not have sufficient efficacy to combat the ATC aggressiveness. Resistance mechanisms appear as a result of the pathway activation by other processes. Moreover, they require a long treatment period before inducing their effects, which is unsafe for patients with a relative survival rate of less than 5 months [20,23–28].

Consistent with the complex therapeutic requirements of the TC and especially of the ATC pathology and based on EGFR overexpression in cancer and its intracellular trafficking [3,10,11,13,16] explained above, the present work aimed to develop by phage display an EGFR-targeted peptide intended to act as a driver of targeted therapies designed for intracellular action, even at the nuclear level. The targeted delivery of drugs to cancer cells limits the contact of therapeutic agents with healthy cells and thus their potential toxic effects. Moreover, combining this molecularly targeted complex with an imaging agent enables the non-invasive monitoring of drug delivery and of therapeutic success by molecular imaging. This approach strives to achieve a balance between efficacy against tumors and minimized toxicity to healthy cells, addressing a critical aspect in the development of safe and effective cancer therapies and enabling a theranostic application.

2. Material and methods

2.1. Phage display technology and peptide synthesis

EGFR-targeted peptides were identified by phage display using a library of randomized linear dodecapeptides (PhD-12, New England Biolabs Inc., Bioké, Leiden, the Netherlands) screened against the extracellular domain (L25-S645) of EGFR (ED-EGFR, Antibodies-online GmbH, Aachen, Germany) as previously described [29,30]. The binding

of phage clones to ED-EGFR was determined by ELISA (HRP anti-M13 monoclonal antibody, Amersham Pharmacia Biotech Benelux, Roosendaal, The Netherlands, 27–9421-01) at a single concentration and based on titration curves aiming to determine their apparent dissociation constant (K^*_d, reflects the dose-dependent binding) and the half-maximal inhibitory concentration in competition with EGF (IC_{50}, reveals the ability to disclose natural ligand from binding sites) [29,30].

The most promising peptides were synthesized (after clone DNA sequencing by Sanger method) either uncoupled or coupled to their N-terminus with chemical moieties like biotin (Eurogentec, Seraing, Belgium), rhodamine (coupling to C-terminus through Lys, LifeTein, LLC, Hillsborough NJ, USA), Texas Red (TR) or IRDye 800CW (SB-Peptide, SmartBioscience SAS, Saint Egrève, France) to allow their observation in *in vitro*, *in vivo* and *ex vivo* models. A small polyethylene glycol molecule (PEG) was placed between peptides and these chemical moieties to reduce the steric hindrance and enable their free interaction with the target. The C-terminus of peptides was amidated to prevent its chemical reactivity.

2.2. Estimation of the K^*_d of selected peptides by ELISA

The K^*_d of selected EGFR-targeted biotinylated peptides was determined by ELISA against ED-EGFR and against a protein of the same family, namely the ED of HER2 (Human ErbB2/Her2, he2-h5212, AA23-652, Antibodies-online). The protocol is similar to that described in [29–31]. The proteins were immobilized (overnight, 4 °C) on ELISA plate at a concentration of 10 μg/mL diluted in immobilization buffer (0.1 M $NaHCO_3$ pH 8,6); Pierce™ Protein-Free (TBS) Blocking Buffer (PFBB, Fisher Scientific, Brussels, Belgium) was used to block the wells. Peptide solutions (in TBS-Tween 0.05 %) with concentrations ranging from 10^{-3} to 10^{-6} M were incubated (100 μL/well) for 2 h at room temperature. Then, the wells were incubated for 1 h with 1 μg/mL of anti-biotin antibody produced in goat (SP-3000), followed by 0.2 μg/mL of anti-goat antibody produced in horse and coupled with peroxidase (PI-9500–1) (both from Vector Labconsult, Brussels, Belgium). The interaction of the peptide with its target was revealed in the presence of a solution of 2,2′-azino-bis-3-ethylbenzothioazoline-6-sulfonic acid, ammonium salt (ABTS, 22 mg%, Sigma-Aldrich, Overijse, Belgium), in 50 mM of sodium citrate pH 4.0, supplemented with 0.5 % of H_2O_2 just before use. OD_{405} was measured with a microplate reader (SpectraMax M2, Molecular Devices, Workingham, Berks, UK).

2.3. Detection by immunohistochemistry (IHC) of EGFR and of peptide binding on human biopsies of thyroid and ATC

The biopsies of healthy human thyroid (10 cases) and of ATC (15 cases) were collected retrospectively and were kindly provided by Drs. Salmon I., Roland I. and Rorive S. (Department of Pathological Anatomy, Erasme Hospital, ULB, Brussels, Belgium).

To assess peptide binding, 20 μM of biotinylated peptide is first incubated overnight with the tissue sections. Then, several successive incubations are carried out with 5 μg/mL of anti-biotin antibody produced in goat (SP-3000), 5 μg/mL of biotinylated anti-goat IgG antibody produced in horse (BA-9500) and the Avidin/Biotinylated enzyme Complex (ABC) Vectastin kit (all from Vector Labconsult). Staining is revealed with 0.05 % of 3,3′-diaminobenzidine (DAB) tetrahydrochloride solution (Sigma-Aldrich) supplemented with 0.02 % H_2O_2. Finally, the counterstaining is achieved with Mayer's hemalum (VWR International, Leuven, Belgium).

To detect EGFR, citrate buffer (10 mM $C_6H_5Na_3O_7{\cdot}2H_2O$, 0.05 % Tween 20, pH 6.0) was used for antigen retrieval. Total EGFR was detected with 1 μg/mL of rabbit monoclonal [EP38Y] anti-EGFR antibody (ab52894), whereas phosphorylated EGFR was identified with 3.21 μg/mL of rabbit monoclonal [EP774Y] anti-EGFR phospho Y1068 (ab40815) antibody (both from Abcam, Cambridge, UK). The secondary antibody was in both cases biotinylated horse anti-rabbit IgG (BA-1100) (Vector Labconsult), which was detected with ABC Vectastin kit and DAB as explained above.

In all tissue sections, the endogenous peroxidases were blocked with 0.7 % H_2O_2 in PBS, biotin was blocked with streptavidin/biotin blocking kit (Vector Labconsult), while unspecific epitopes were blocked with PFBB.

After Mayer's hemalum counterstaining, tissue sections were mounted with acrytol mounting medium (Surgipath®, Leica Biosystems, Diegem, Belgium) and observed on a DM2000 Leica microscope equipped with a DFC 425C camera (Leica Microsystems, Groot Bijgaarden, Belgium). At least five microphotographs were acquired for each histological section and were analyzed semi-quantitatively with ImageJ software (National Institutes of Health, USA) by measuring the percentage area of stained biomarker using the particle analysis tool [31,32]. The results were normalized to the blank sample (where the biotinylated peptide or the primary antibody were excluded) and expressed as the Relative Ratio of IHC Labeling (RRIL).

2.4. Cell lines and culture

The cellular effects of peptides and their endocytosis were assessed on 8505c (undifferentiated thyroid carcinoma, European Collection of Authenticated Cell Cultures (ECACC) 94090184) and Cal-62 (thyroid anaplastic carcinoma, DZMZ-German Collection of Microorganisms and Cell Cultures, ACC 448) TC cell lines (both kindly provided by Prof. Sven Saussez). Nthy-ori 3–1 (normal human primary thyroid follicular epithelial cells, ECACC 90011609, Culture Collections, Public Health England, UK, Sigma-Aldrich) cell line was used as control. The 8505c and Nthy-ori 3–1 cell lines were grown in RPMI 1640 (Roswell Park Memorial Institute 1640) culture medium, while DMEM was used to culture Cal-62 cells. In both cases, the culture medium was supplemented with 1 % Glutamax, 1 % antibiotics (Penicillin/Streptomycin) and 10 % Fetal Bovine Serum (FBS) (all from Fisher Scientific) and the cells were cultured at 37 °C and 5 % CO_2.

2.5. Experimental conditions and techniques assessed on cells

The cells were seeded and cultured in multi-well culture containers (4-well culture slides for microscopy, Falcon®, VWR, Leuven, Belgium; 6-well, 24-well or 96-well culture plates for Western Blot, ELISA and flow cytometry studies, Greiner Bio-One, Vilvoorde, Belgium) in order to obtain on the day of the experiment 4–5 × 10^5 cells/well (for immunofluorescence (IF) and flow cytometry), 3 × 10^6 cells/well (for Western Blot), 6 × 10^5 cells/well (for ELISA/AKT) or 6 × 10^4 cells/well (for ELISA/BAD). The effect of peptides on EGFR endocytosis and expression was investigated by IF and Western Blot on cells grouped in four experimental conditions incubated all in FBS-free culture medium supplemented or not with various compounds, as follows: (1) cells incubated in culture medium alone (i.e., in the absence of EGF or peptides); (2) cells stimulated with 1 μM EGF (Sigma-Aldrich); (3) test condition incubated with 40 μM of peptide; (4) test condition incubated with 1 μM EGF and 40 μM of peptide. Condition 2 was pre-incubated with FBS-free culture medium and condition 4 was pre-incubated with 40 μM peptide for 30 min (for EGFR expression studies) or with 1 μM EGF for 2 h (for peptide-rhodamine or peptide-TR colocalization with EGFR or with cell compartments, such as ER, nuclei, and caveolae). The cells were then incubated (37 °C, 5 % CO_2) for 2 h (for EGFR, AKT and BAD expression studies) or for 1 h (for peptide-EGFR colocalization, endocytosis and life survival studies). To corroborate the specific mechanism of endocytosis, the selected peptide was preincubated for 30 min with 80 nM ED-EGFR (Antibodies-online GmbH) in solution before adding it to the conditions 3 and 4 and continuing the incubation for 1 h; cells in conditions 3 and 4 were preincubated with 1 μM of EGF for 2 h.

2.5.1. Studies performed by IF

After treatment, the cells were fixed with methanol for 10 min at

−20 °C, then they were blocked with PFBB for 1 h. Total EGFR expression was determined with 0.52 μg/mL of EP38Y antibody, while phosphorylated EGFR (EGFR-pY1068) was observed with 3.21 μg/mL of EP774Y antibody (both from Abcam). The primary antibodies bound to their target were detected with 15 μg/mL of horse anti-rabbit IgG (H + L) Dylight™ 488 (DI-1088, Vector Labconsult). Finally, the cells were mounted with mounting medium for fluorescence with DAPI (VECTASHIELD® Vibrance®, Vector Labconsult).

For the colocalization of EGFR with ER, the ER-ID Green solution (Enzo Life Sciences, Brussels, Belgium) was applied for 30 min at 37 °C after incubation of cells with antibodies for EGFR detection. Finally, the cells were mounted with PBS.

To colocalize EGFR-targeted peptide with ER, the cells previously incubated with peptide-TR as described above were then fixed for 15 min in 4 % formaldehyde at room temperature, followed by 10 min incubation with methanol at −20 °C. After blocking them for 1 h with PFFB, ER-ID Green containing Hoechst (Enzo Life Sciences) was applied for 30 min at 37 °C. Finally, the cells were mounted with PBS.

For the colocalization of peptide-TR with caveolae, the cells were treated and fixed as described above and then they were incubated with rabbit polyclonal anti-caveolin-1 primary antibody (4 μg/mL, sc-894, Santa Cruz Biotechnology, Heidelberg, Germany) at 4 °C overnight, followed by incubation with goat anti-rabbit secondary antibody coupled to fluorescein (20 μg/mL, FI-1000, Vector Labconsult) at room temperature for 1 h. Finally, cells were mounted with mounting medium for fluorescence with DAPI.

The slides were observed with the fluorescence microscope Leica DM2000 equipped with an EL6000 fluorescence light source and a DFC 425C camera (Leica Microsystems, Groot Bijgaarden, Belgium). At least five microphotographs for each biomarker and five for the nuclei were acquired for further analysis.

The fluorescent labeling of cells and the effect induced by the peptides were expressed by the Relative Ratio of Fluorescent Labeling (RRFL). This takes into account the fluorescent labeling evaluated semi-quantitatively using the ImageJ software. Results (provided as means by ImageJ) were normalized to nuclei count, blank (not incubated with primary antibody or fluorescent peptide), and cells stimulated with EGF (when the effect of peptide on EGFR expression or activation was studied). The overlap between the pixel intensities of various biomarkers was also analyzed with ImageJ by using the Coloc2 plugin, which provides several colocalization coefficients, such as Manders' and Pearson [33].

2.5.2. Studies performed by Western Blot

After incubation in culture conditions, the cells were collected, rinsed and centrifuged before being lysed using RIPA lysis and extraction buffer supplemented with cocktails of protease and phosphatase inhibitors (all from Fisher Scientific) according to the manufacturer's protocol. The protein concentration of each sample was determined using the Pierce BiCinchoninic Acid (BCA) protein assay kit (Fisher Scientific). Twenty μg of proteins per sample were denatured for 5 min at 95 °C in the loading buffer comprising 1x LDS (NuPAGE™, LDS Sample Buffer, Fisher Scientific), 2 mM dithiothreitol (DTT) and ultrapure water in a total volume of 25 μL. The protein migration was performed by electrophoresis at 120 V for 70 min in precast gels (4–20 % Mini-PROTEAN® TGX™ Gels 10 wells, BIO-RAD, Temse, Belgique) immersed in Tris/glycine/SDS running buffer. PageRuler™ Prestained Protein Ladder 10–180 kDa (Fisher Scientific) was used as protein size standard. After electrophoresis, the gel was first incubated for 5 min in the Tris/glycine/methanol transfer buffer before transferring the proteins (iBlot™, 2 Dry Blotting System, Fisher Scientific) on nitrocellulose paper (iBlot® 2 NC Regular Stacks, nitrocellulose, Fisher Scientific) presoaked in Tris/glycine/methanol transfer buffer. The membrane was then blocked for 5 min in EveryBlot Blocking Buffer (BIO-RAD) before overnight incubation at 4 °C with 0.104 μg/mL of EP38Y antibody or with 0,877 μg/mL of EP774Y antibody. Next day, the membrane was incubated (1 h, room temperature) with 1 μg/mL of goat anti-rabbit IgG coupled with peroxidase (PI-1000, Vector Labconsult), followed by 5 min incubation with chemiluminescent substrate solution (Novex™ ECL Chemiluminescent Substrate Reagent Kit, Fisher Scientific) and imaging with Bioimager Fusion FX (Vilber Lourmat, France). β-actin was detected as a loading control protein using 1 μg/mL of mouse anti-β-actin antibody (sc-47778, Santa Cruz Biotechnology) and 2 μg/mL of goat anti-mouse IgG coupled to HRP (ab6789, Abcam). Finally, the Western Blot bands were semi-quantitatively analyzed by densitometry using the ImageJ software, the results being normalized to the density of the β-actin band.

2.5.3. Quantification by ELISA of total and phosphorylated (pSer473 and pThr308) AKT

The cells were seeded, cultured and treated as described above, but only the conditions 1 and 3 were assessed. After treatment, the cells were recovered, lysed and proteins extracted using the Cell Lysis Buffer Mix of the kit ELISA-AKT 1/2/3 (Total/Phospho) InstantOne ELISA™ in the case of total and pSer473 AKT, or in Cell Extraction Buffer supplemented with 1 mM phenylmethylsulphonyl fluoride (PMSF, a serine protease inhibitor) and cocktails of protease and phosphatase inhibitors in the case of AKT-pThr308 (AKT (Phospho) [pT308] Human ELISA Kit). Total protein was determined in each sample using the BCA protein assay kit (all from Fisher Scientific) and used for the normalization of AKT results.

The two kits used for the AKT quantification are based on sandwich ELISA, where the sample (110 μg protein/mL) is concomitantly incubated with the capture antibody and the detection antibody in one single step (in the case of AKT 1/2/3 (Total/Phospho) InstantOne ELISA) or they are successively incubated with the sample (110 – 400 μg protein/mL), the capture antibody being pre-immobilized on ELISA plate (in the case of AKT-pThr308 (AKT Phospho) [pT308] Human ELISA Kit). The chromogen substrate was 3,3′,5,5′-Tetramethylbenzidine (TMB) provided by the kit supplemented with H_2O_2 in both cases and was provided by the kits. After adding the stop solution, OD_{450} was measured with a microplate reader (SpectraMax M2).

2.5.4. Quantification by ELISA of total and phosphorylated (pSer136) BAD

The cell treatment with conditions 1 and 3 was carried out in 96-well culture plates provided by the kits Phospho-Ser136 Colorimetric Cell-Based ELISA and Bad (Bcl2 associated agonist of cell death protein) Colorimetric Cell-Based ELISA (Boster Bio, Sanbio BV, Uden, Pays-Bas), which are based on cellular ELISA principle. The cells were fixed with 4 % buffered formaldehyde, the endogenous peroxidase blocked with a kit reagent, followed by the incubation (overnight, 4 °C) with the primary antibodies, including the one against the glyceraldehyde-3-phosphate dehydrogenase (GAPDH) detected as an internal control. Next day, the cells were incubated (1 hour 30 min, room temperature) with the secondary antibodies, followed by the chromogen substrate (TMB/H_2O_2) and the stop reagent (H_2SO_4 2 N). After reading the OD_{450} with a microplate reader (SpectraMax M2), the wells were rinsed and dried, and then the cells were stained with crystal violet, followed by dissolution with SDS (all provided by the kit) and OD_{595} measurement with a microplate reader (SpectraMax M2). The OD_{450} data were normalized to OD_{595} results and finally to the GAPDH measurements.

2.5.5. Quantification of life survival by flow cytometry

After growing and treating the cells with conditions 1 and 3, they were rinsed and then incubated (20 min, room temperature) with the Muse® reagent of the Annexin V & Dead Cell kit (Luminex®, DiaSorin Company, MV's-Hertogenbosch, The Netherlands), which enables the detection of phosphatidylserine (PS)-bound Annexin V in the early stages of apoptosis. A dead cell marker (7-ADD) is also present to detect cells in late apoptosis or dead; it is an indicator of membrane integrity and is therefore excluded from living cells or cells in early apoptosis.

After incubation, the samples were placed in the Muse cell analyzer

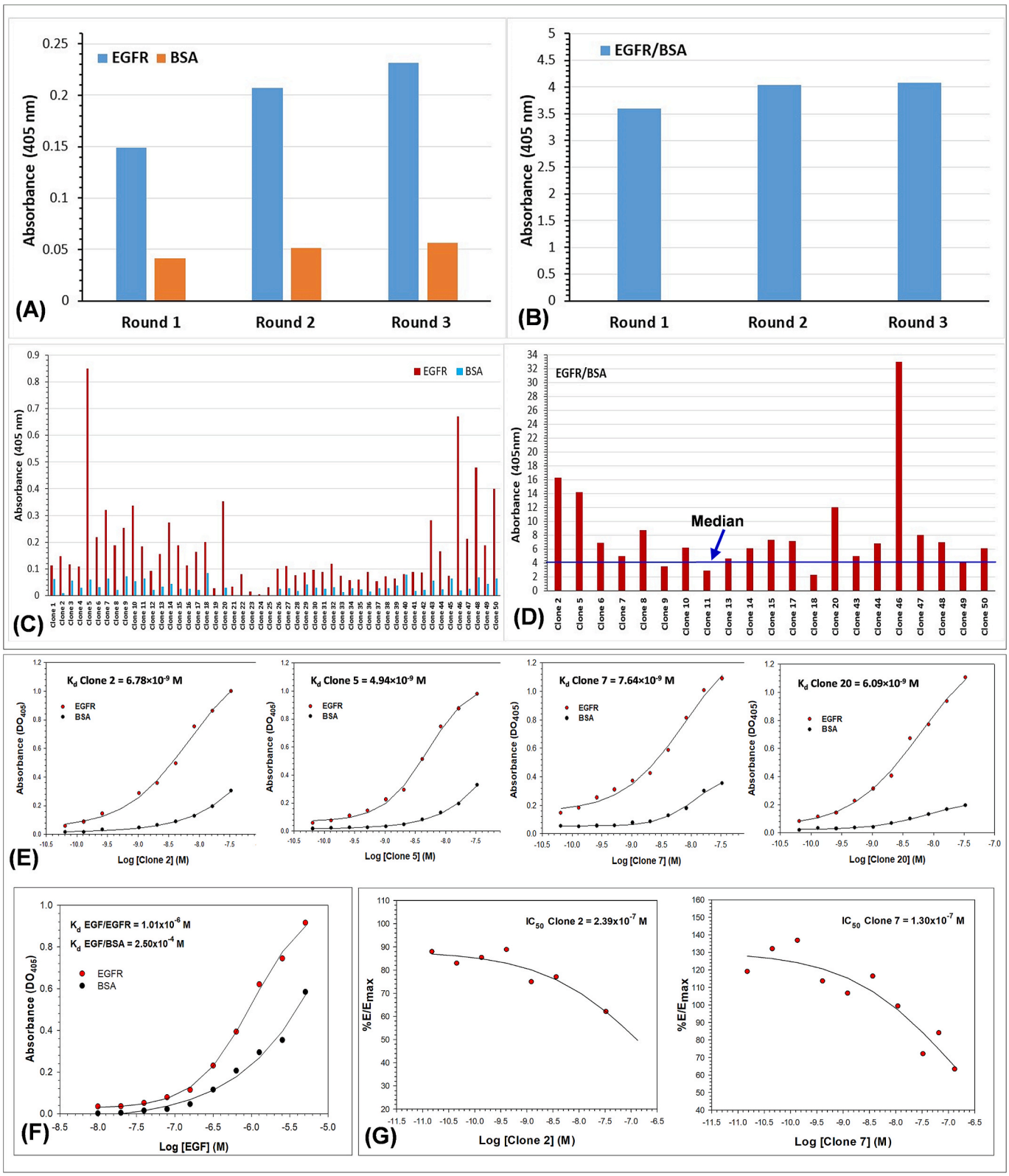

Fig. 1. Summary of the results acquired during the phage display screening. (A) Binding to the target and to BSA of the phage pools obtained after three rounds of panning; (B) EGFR/BSA ratio of the different phage pools; (C) Binding of the 50 phage clones towards the target and BSA; (D) Selection of the 21 phage clones with the best affinity to the target; (E) The titration curves and K^*_d values against EGFR and BSA of peptide clones 2, 5, 7 and 20; (F) The titration curve and K^*_d value of EGF. (G) The titration curves and IC_{50} values of peptide clones 2 and 7.

Table 1
Amino acid sequences of the 21 selected clones and their theoretical biochemical parameters estimated *in silico* via the ExPASy Protparam computer tool.

Parameter	Sequence 1 (P2)	Sequence 2 (P5)	Sequence 3 (P7)	Sequence 4 (P20)
Peptide sequence	Asp-Tyr-His-Asp-Pro-Ser-Leu-Pro-Thr-Leu-Arg-Lys	Asp-Asp-His-Asp-Pro-Ser-Leu-Pro-Thr-Leu-Arg-Lys	Val-Gln-Glu-Asp-Pro-Thr-Gln-Arg-Pro-Arg-Arg-Lys	Val-His-Leu-Glu-Tyr-Asn-Thr-Ser-Thr-Ala-Pro-Thr
Clones	2	5–6-8–9-10–11-13–14-15–17-18–43-44–46-47–48-49–50	7	20
pI	6.75	5.3	10.74	5,24
A.I.	65.00	65.00	24.17	65.00
Half-life	1.1 h	1.1 h	100 h	100 h
AA %				
Acid	16.7	25	16.7	8.3
Basic	25	25	33.33	8.3
Non-polar	33.3	33.3	25	33.3
Polar	25	16.7	25	50

pI: isoelectric point; A.I.: aliphatic index; half-life: theoretical half-life time (estimated according to the amino acid expressed at the N-terminal end of a polypeptide chain); AA%: amino acid composition expressed as a percentage.

(Guava® Muse®) device for analysis. Four cell populations were thus detected: live cells, Annexin V(−) and 7-AAD(−); early apoptotic, annexin V(+) and 7-AAD(−); late apoptotic, annexin V(+) and 7-AAD (+); cellular debris or dead cells, annexin V(−) and 7-AAD(+).

2.6. Studies performed in vivo

The *in vivo* studies were approved by UMONS Animal Care and Use Committee (project SA-04–03) in agreement with the guidelines specified by EU directive (2010/63/EU) and the animal welfare service of SPF Wallonia (Agreement: LA1500549). The goals of these studies were to observe the eventual toxic effects produced by the selected EGFR-targeted peptide, as well as its tumor homing in a mouse model of ATC. During all experiments, the animals had ad libitum access to the food and drink intake.

2.6.1. Studies of toxicity

NMRI female mice (35–41 days-old, n = 4 per group; Charles River Laboratories, Saint Germain Nuelles, France) were injected i.v. (caudal vein) with 200 nmol/kg b.w. of EGFR-targeted peptide after being anesthetized either with 0.3 L/min of 2 % isoflurane or with i.p. injection of 100 mg/kg of ketamine hydrochloride (Nimatek, Eurovet Animal Health B.V., Ireland). Physiological serum (0.9 % NaCl) was administered to negative control mice. Animals were treated three times per week for 3 weeks. Finally, they were sacrificed by i.p. injection of 200 mg/kg of Dolethal (VETOQUINOL SA, Ireland) before collecting the blood (on heparin) and organs (heart, lungs, intestine, liver, kidneys) for further investigations.

Blood plasma was isolated by centrifugation (7000 rpm, 30 min), whereas the tissues were harvested after transcardial perfusion with PBS [31,32]. They were then fixed in 4 % paraformaldehyde for 24 h before dehydration in alcohol and butanol and final embedding in paraffin. Slices of 5 μm thickness were finally cut for morphology studies after Masson's Trichrome staining (Mayer's hematoxylin, ponceau xylidine dye, aniline acetate, phosphotungstic acid) performed at the DIAPath (Digital Image Analysis in Pathology) platform of the Center for Microscopy and Molecular Imaging (CMMI, Gosselies, Belgium). Apoptosis was detected in livers using 5 μg/mL of rabbit anti-active caspase-3 antibody (9H19L2) (15336944, Fisher Scientific) followed by 15 μg/mL of horse anti-rabbit antibody coupled to Dylight 488 (DI-1088, Vector Labconsult). Liver slices were finally mounted with mounting medium for fluorescence with DAPI (VECTASHIELD® Vibrance®, Vector Labconsult).

Alanine aminotransferase (ALT) and aspartate aminotransferase (AST), total cholesterol (T-Chol), total bilirubin (T-Bil), blood urea nitrogen (BUN) and glucose were measured in plasma using SPOTCHEM II Multi Panel-1 kit (ARKRAY, Inc, Kyoto Japan) based on the manufacturer's protocol. A SPOTCHEMTM EZ SP-4430 equipment (ARKRAY, Inc, Kyoto Japan) was employed for the measurement of these biomarkers.

2.6.2. Studies by fluorescence imaging (FLI)

The biodistribution in tumors of our EGFR-targeted peptide coupled with IRDye 800CW (IRDye800-P20) was studied *in vivo* on female athymic nude mice (42–48 days-old at the beginning of the study, NU (NCr)-Foxn1^{nu}, Charles River Laboratories) bearing 8505c tumors. To obtain tumors, 100 μL of culture medium free of FBS and containing 8×10^6 8505c cells (cultured as described above) were xenografted s.c. in the right thigh. Three weeks later, the tumors attained a volume of 1235 ± 756 mm^3.

During FLI studies (performed at the Non-Ionising Molecular Imaging, NIMI, platform of CMMI), mice were anesthetized with 0.3 L/min of 2 % isoflurane and the images were acquired with a PhotonIMAGER Optima (Ex. = 712 nm, Em. = 797 nm, TA = 5 sec; Biospace Lab, Nesles la Vallée, France) using 4-views module before and after (30 min, 60 min, 120 min) the i.v. (caudal vein) injection of 1.2 μmol/kg b.w. of IRDye800-P20 (n = 3 mice) or of 2.4 μmol/kg b.w. of P20 alone followed by 1.2 μmol/kg b.w. of IRDye800-P20 10 min later (n = 4 mice). The results of signal intensity (SI) measurements on tumors were normalized either to the pre-dye SI or to the SI measured on contralateral thigh and expressed in percentage [34]. After imaging studies, the mice were euthanized with Dolethal, while tumors and organs (as described above) were collected for IHC detection of EGFR-pY1068 and total EGFR.

2.7. Statistical analysis

All studies were performed in at least experimental triplicates and several technical replicates. The results were statistically analyzed using the SigmaPlot 12.0 software, which checks first the normality of the data by the Shapiro-Wilk test. If the data follows an abnormal distribution, the software applies the Mann-Whitney test, and the results are then represented in box-and-whiskers plots. For the normal distribution of the data, the software uses the Welch's *t*-test if the variances are not equal or the Student's *t*-test if the variances are equal; these results are represented as means ± standard deviation (SD) in histograms. The differences between groups are considered significant when the p-value is of at least $p < 0.05$.

3. Results

3.1. Phage display screening, phage clone selection and DNA sequencing

After three rounds of bio panning, the affinity of each phage pool output towards the ED-EGFR increased progressively, presenting a

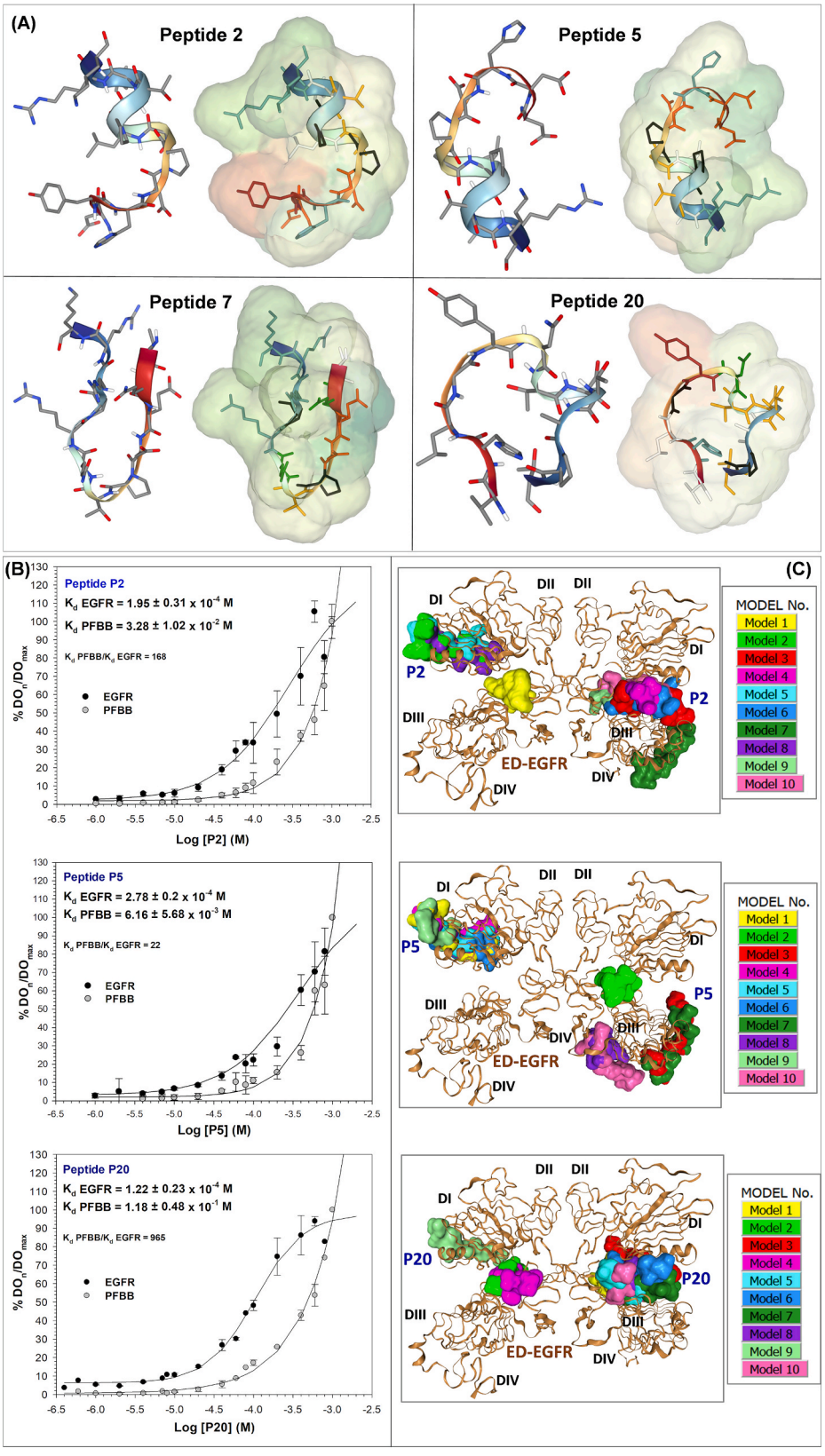

(caption on next page)

Fig. 2. Structure and affinity characteristics of the candidate EGFR-targeted peptides. (A) Three-dimensional structures of the four potential vector peptides (P2, P5, P7 and P20) and their solvent accessible surfaces as determined using the PEP-FOLD 4 web software (https://bioserv.rpbs.univ-paris-diderot.fr/services/PEP-FOLD4/) [35]; (B) The titration curves and K^*_d of the three selected peptides (from up to down: peptides P2, P5 and P20). The binding rate of each peptide to the ED-EGFR or to the blocking agent (PFBB) is expressed as a percentage of absorbance values measured at different peptide concentrations ($\%OD_n$) relative to the maximum binding (OD_{max}) measured at the highest peptide concentration. Results are presented as means ± SD; n = 3. (C) Prediction models for binding between the dimerized extracellular domains of EGFR (in brown) and the vector peptides (from up to down: peptides P2, P5 and P20) shown in different colors according to the legend (models 1 to 10), determined by the HPEPDOCK web server (http://huanglab.phys.hust.edu.cn/hpepdock/); the extracellular regions of two EGFR monomers are shown, with DI to DIV corresponding to the four EGFR domains. The crystallographic structure of ED-EGFR is provided by the server after the introduction of the protein Protein Data Bank (PDB) identification number, i.e. the A/B chains of the PDB 1IVO model [36].

negligible binding to BSA (Fig. 1A). The ratio ED-EGFR/BSA (Fig. 1B) reveals an increase in ED-EGFR-specific binding from the first round to the second and third rounds, where a plateau appears. Based on these results, 50 clones were randomly isolated from the pool of the third round. Their affinity to the target was assessed using an ELISA test, showing that all clones exhibit higher affinity to the target relative to the BSA (Figs. 1C and 1D). Among them, 21 are selected according to arbitrarily chosen criteria, i.e., those with an absorbance measured on ED-EGFR $\geq$ 0.15 and/or a ratio ED-EGFR/BSA $\geq$ 4.28 (corresponding to the median).

The DNA sequencing of the 21 selected clones revealed the expression of 4 different peptides, one expressed by 18 clones and the other 3 sequences each expressed by a single clone (Table 1). The 3D structures of these peptides, their spatial conformation and interaction with the solvent are available in Fig. 2A. The ExPASy proteomics server (sequence analysis tool) was used to analyze the primary structures of peptides, allowing to obtain their theoretical biochemical characteristics (Table 1).

The aliphatic index, which is defined as the relative volume occupied by the aliphatic side chains (Ala, Val, Ile and Leu), of the EGF (N^{971}-R^{1023}) is 71.7. Sequences of P2, P5 and P20 have an aliphatic index close to that of EGF. Conversely, the sequence of P7 has a lower aliphatic index than that of EGF. The theoretical half-life time is 1.1 h for the first two sequences (1.4 h for EGF) and 100 h for the last two sequences. These half-life times are long enough for the peptides to exert their activity at the cellular level before they are degraded at the proteasome level.

The amino acids of EGF responsible for its interaction with EGFR are mostly charged (acid or basic function) or carry an alcohol on their side chain and establish hydrogen bonds (Tyr^{44}, Gly^{39}, Glu^{40}, Cys^{33}, Asp^{46}, Ala^{25}, Arg^{41}, Arg^{45}, Glu^{51}, Trp^{50}) and/or salt bridges (Glu^{39}, Arg^{41}, Asp^{46}, Lys^{48}, Glu^{51}, Lys^{28}) [37]. Our peptide sequences are formed mainly by Asp, Lys, Arg and His, which are charged amino acids and Ser, Thr and Tyr which have an alcohol function. These amino acids can contract hydrogen bonds or salt bridges. Sequences of P2, P5 and P7 are rather formed by charged amino acids while P20 sequence is formed mainly by amino acids with an alcohol function.

The K^*_d of clones expressing the peptides of interest (Table 1) was evaluated to study the binding between the clones and the EGFR target, BSA being used as a negative control (Fig. 1E). Clones 5 and 20 show slightly lower K^*_d values for ED-EGFR binding than the other two sequences, suggesting a better affinity. The affinity of clones towards BSA is negligible because the absorption values are in the background domain. The K^*_d of EGF to ED-EGFR is 1.01×10^{-6} M (Fig. 1F). This value is higher than that reported by the specialized literature (1 – 100 nM) [37] and could be explained by the analytical method used to evaluate K^*_d.

The IC_{50} curves obtained for clones 2 and 7 (Fig. 1G) reveal that the binding of EGF to ED-EGFR is decreased as the clone concentration increases. This means that these clones are competitors, with clone 7 being slightly more efficient with an IC_{50} of 1.30×10^{-7} M. The curves of clones 5 and 20 are not shown because the binding of EGF to EGFR is 100 % despite the presence of clones. This means that these clones do not prevent the EGF binding to the target. These clones are therefore non-competitive. The aim of this work is to develop peptides that allow the delivery of the drug without interfering with the EGFR pathway. It is for this reason that the peptides selected for synthesis are those expressed by clones 5 and 20. Indeed, these clones are not competitors of EGF, and they have a low K^*_d, which reflects their good affinity towards the target. Peptide expressed by clone 2 was also synthesized for a primary evaluation of its effect on cells.

3.2. *In vitro evaluation of the three candidate peptides*

The three candidate peptides (P2, P5 and P20) have a K^*_d value against ED-EGFR in the range of 10^{-4} M (Fig. 2B). P20 exhibits a stronger affinity than P2, which in turn has a stronger affinity than P5. The binding of peptides to the blocking agent PFBB is weak, P20 showing a negligible affinity given its K^*_d of 1.18×10^{-1} M. The affinity of peptides to ED-EGFR is 168 times higher for P2, 22 times higher for P5, and 965 times higher for P20 compared to their affinity to PFBB. This means that P20 has a specific affinity towards EGFR, which makes it the best candidate according to the results of this test. Subsequent *in vitro* characterization studies were performed using P20 concentrations of 20 μM or 40 μM, which are lower than its K^*_d value and correspond to those used for other peptides evaluated in our previous work [29,30].

The molecular mechanisms of the binding of the three candidate peptides to EGFR were analyzed *in silico* by peptide-protein docking studies using the HPEPDOCK web server (http://huanglab.phys.hust.edu.cn/hpepdock/) [38]. The top 10 models predicted by the program were visualized for each peptide to determine which ED-EGFR domain is preferentially bound by each one of them (Fig. 2C). Thus, P2 binds to all ED-EGFR domains, with 3 models in domain I, 1 model in domain II, 1 model in domain III, and 5 other models between domains I and III out of the top 10 predicted by the program. P5 also binds to all EGFR domains with 5 models in domain I, 1 model in domain II (between domains I and III), and 4 models between domains III and IV. P20 binds preferentially between domains I and III according to 9 of the top 10 predicted models. It is interesting to recall that EGF binds between domains I and III of ED-EGFR. P2 (5 out of 10 models) and particularly P20 (9 out of 10 models) are more likely to bind between domains I and III. Our analysis have shown that peptides interact with ED-EGFR in the same regions as EGF, but not necessarily with the same amino acids as EGF. They also interact with regions where EGF does not interact with the receptor. The predominant type of EGF interaction with ED-EGFR is hydrophobic bonding, whereas our peptides are more likely to contract salt bridges and hydrogen bonds.

Subsequently, the effect of peptides on a cellular model of ATC (i.e., 8505c cells) was determined by IF detection of activated EGFR, evaluated by observing the Tyr^{1068} phosphorylation (EGFR-pY1068) (Fig. 3A). EGFR-pY1068 was studied on cells non-stimulated or stimulated with EGF and incubated or not with P2, P5 or P20. Green immunostaining was found at the membrane, cytoplasmic and nuclear levels. This cellular distribution is explained by EGFR endocytosis after its activation, followed by its recycling to the membrane surface, lysosomal degradation or translocation into cellular compartments, such as the nucleus, mitochondria and ER [10,11]. Moreover, a significant nuclear distribution of activated EGFR is observed with EGF, P2 and P5 (Fig. 3A).

Treatment with P2 shows more intense labeling than that of the cells not stimulated with EGF, which suggests EGFR activation. These results corroborate the data presented above, which revealed the competitive

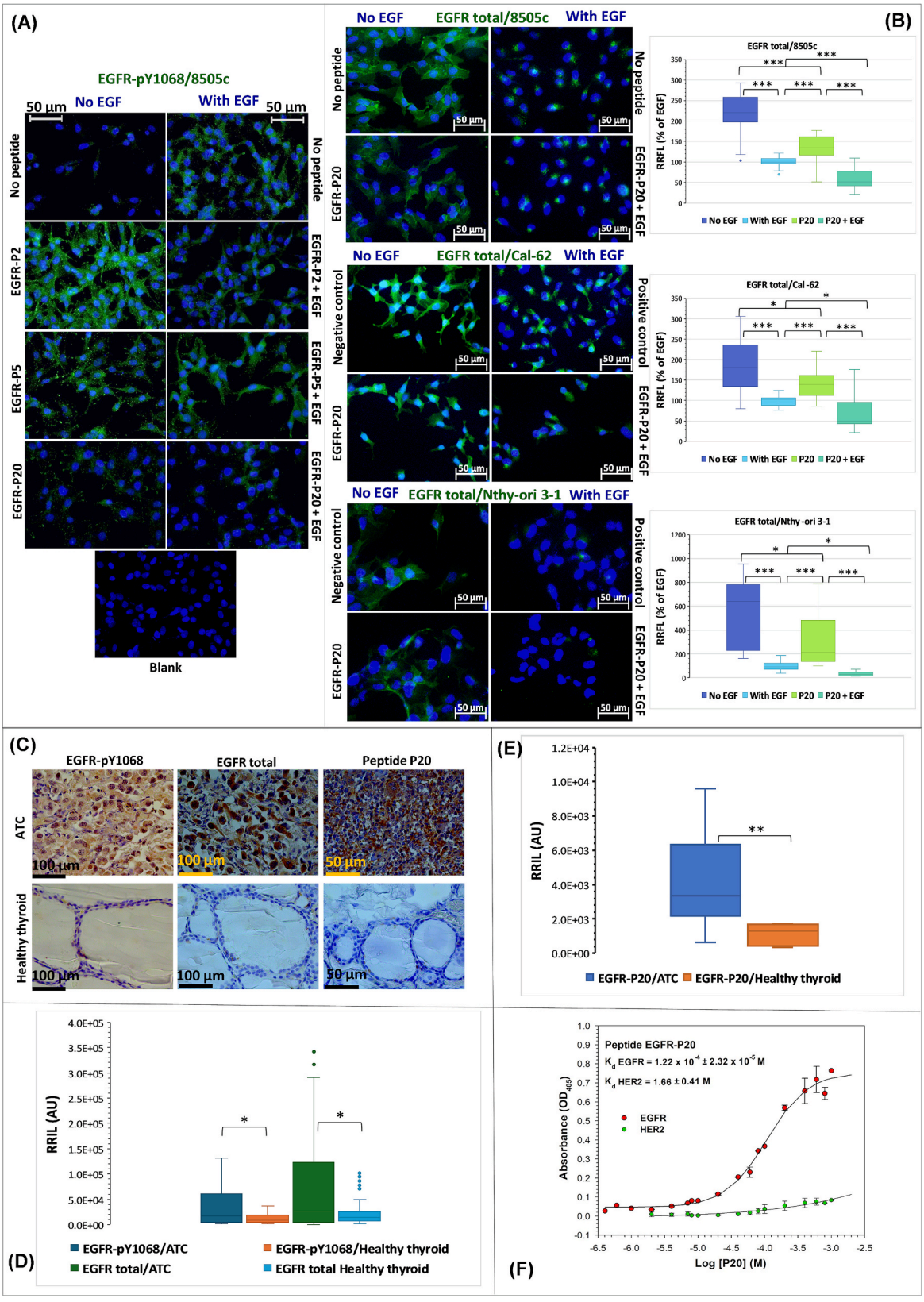

(caption on next page)

Fig. 3. *In vitro* characterization of the selected peptide candidates. (A) IF detection of EGFR-p1068 on 8505c cells treated for 2 h with different conditions, i.e., culture medium alone (No EGF), 1 μM EGF (With EGF), 40 μM of peptides P2, P5, P20 alone or co-incubated with EGF (from up to down). EGFR-pY1068 is labelled green with fluorescein; cell nuclei are labelled blue with DAPI. The number of replicates were n = 3/condition, except P20, where n = 9; 15–45 technical replicates. (B) IF detection of total EGFR and effect of P20 peptide on its expression by 8505c, Cal-62 and Nthy-ori 3–1 cell lines (from up to down in the left panel). The corresponding RRFL is expressed as percentage of EGF-stimulated cells and is represented for each cell line on the box-and-whisker plots shown on the right panel. The number of replicates were n = 3/condition, 15 technical replicates. The statistical difference between the experimental conditions is assessed by the Mann-Whitney test: *: $p < 0.05$; ***: $p < 0.001$. (C) Detection by IHC of EGFR-pY1068 and of total EGFR, and the binding of biotinylated peptide P20 on human biopsies of ATC (n = 15, 5 pictures per case and condition) and healthy thyroid (n = 10, 5 pictures per case and condition). EGFR is stained in brown, highlighted by DAB. The semiquantitative analysis (RRIL) of EGFR expression (D) and of P20 binding (E) is shown in box-and-whisker plots where the statistical differences between ATC and healthy cases were determined by the Mann-Whitney test. *: $p < 0.05$; **: $p < 0.01$. (F) The titration curve and K^*_d of P20 towards ED-HER2 (green) compared to ED-EGFR (red). Results are presented as means ± SD; n = 3 per titration curve.

nature of the P2, being able to act as an EGFR agonist. However, in the presence of EGF, P2 does not have a synergistic effect. P5 seems to have a similar effect on EGFR activation, but at a lower level in the absence of EGF. Its non-competitive nature may explain the absence of an effect in cells stimulated with EGF.

The photos reveal a very low immunostaining in the P20 presence and even less with the addition of EGF. We have already considered P20 as the best likely candidate given its selectivity and non-competitive property. The present results suggest that it also decreases the EGFR phosphorylation and acts as a non-competitive inhibitor, with the potential to improve the therapeutic effect of an anti-cancer drug. Based on the results obtained so far, P20 is the best candidate as a vector peptide. Docking studies as well as theoretical biochemical property analysis also positioned P20 as the ideal EGFR-targeted peptide, which justified our decision to pursue its *in vitro* and *in vivo* characterization.

3.3. The effect of peptide P20 on total EGFR expressed by cells observed by IF

The effect of P20 on total EGFR expression was studied by IF on two thyroid cancer cell lines (8505c and Cal-62) and one healthy thyroid cell line (Nthy-ori 3–1) in cells not-stimulated or stimulated with EGF (Fig. 3B). All the following observations can be assimilated to the three cell lines.

A decreased expression of total EGFR can be observed in cells exposed to EGF, and this is true in the presence or absence of P20. In addition, EGFR is mainly localized at the plasma membrane in non-stimulated cells, and rather intracellular (vesicles close to the nucleus) in cells stimulated with EGF due to its endocytosis as explained above. This endocytosis is accompanied by a decreased EGFR expression, which could be partly explained by its degradation in lysosomes.

By comparing the non-stimulated cells without P20 and with P20, we observe a decreased expression of total EGFR. Then, by comparing the EGF stimulated cells without P20 with those incubated with P20 (P20-EGF), we also observe a decreased expression of total EGFR, which confirms the hypothesis that P20 would be able to induce EGFR endocytosis in addition to the effect of EGF.

Finally, we can compare the decrease in total EGFR expression based on the addition of P20, EGF, or both versus non-stimulated cells. We notice that the presence of P20 alone induces a decreased expression of total EGFR, but not as much as EGF which is normal because EGF is the natural ligand of EGFR. On the other hand, when P20 and EGF are present simultaneously, the decreased expression of total EGFR is even greater than in the two previous cases. This then confirms the hypothesis that P20 is capable of inducing EGFR endocytosis but not as much as its natural ligand, EGF.

3.4. Expression of EGFR by human biopsies and binding of P20 determined by IHC

Before confirming the binding of P20 to the EGFR expressed by human tissue, its presence in various cases of ATC was validated to confirm the role of EGFR as a biomarker for drug delivery. Indeed, the overexpression of EGFR is reported in many cancers, including TC, since the underlying signaling pathway triggered by EGFR regulates tumor proliferation, cell survival, and neo-angiogenesis, all of them being necessary for tumor development [2,11,14,16].

The IHC staining of EGFR-pY1068 and of total EGFR in human biopsies studied in this work shows that EGFR labeling is obviously more important in cases of ATC than in those of healthy thyroid (Fig. 3C). The staining is heterogeneous and rather diffuse, likely due to the presence of two histological categories of ATC, which can coexist within the same tumor [39]. The sarcomatoid category is characterized by spindle cells and giant cells. Giant cells present hyperchromatic nuclei, significant eosinophilic cytoplasm, and a round or oval shape. Histological markers suggestive of sarcomatoid anaplastic cancer are significant pleomorphism, strong mitotic activity, and significant necrosis. The second category, epithelioid-squamoid, has a less heterogeneous histological appearance than sarcomatoid tumors. Cells in this category are polygonal with an epithelial appearance. Looking at the different cases of ATC in our study, it seems that areas of sarcomatoid ATC present higher EGFR labeling compared to areas of epithelioid-squamoid ATC. The immunostaining produced by biotinylated peptide P20 presents a comparable pattern of distribution as that obtained with antibodies, especially with the one that detects total EGFR, which binds the ED-EGFR.

The semi-quantitative analysis of EGFR staining was performed using the ImageJ software, both for antibodies (Fig. 3D) and biotinylated P20 (Fig. 3E). This analysis confirms that EGFR is indeed overexpressed and overactivated ($p < 0.05$) in ATC as compared to healthy thyroid, corroborating the literature [16]. This significant difference between ATC and healthy thyroid ($p < 0.01$) is also observed for P20 immunostaining.

3.5. Specific binding of P20 to ED-EGFR

The studies presented above suggested that P20 presents a specific binding to EGFR. During the next step of evaluation, we deepened this specificity study by investigating its potential binding to ED-HER2 (belonging to EGFR family of proteins) by determining its K^*_d (Fig. 3F).

HER2 is an orphan receptor that plays the role of co-receptor and increases the affinity of ligands towards dimerized receptors by forming highly active heterodimers with its counterparts [1,2,40]. In addition, overexpression and amplification of HER2 have been observed in breast, stomach, esophageal, endometrial and thyroid cancers, being associated with severe prognosis [40,41].

This study showed that P20 has negligible affinity for ED-HER2, consistent with its K^*_d value of 1.66 M. The K^*_d of P20 towards ED-EGFR is 1.22×10^{-4} M, which is 13,606 higher than its affinity to ED-HER2, confirming the specific binding of P20 to ED-EGFR.

3.6. Intracellular colocalization of P20 with total EGFR observed by IF

Aiming to determine the intracellular trafficking of P20 once endocytosed in cells, we studied its colocalization with the EGFR receptor (Fig. 4A), which was estimated based on the Manders' coefficient. P20-rhodamine colocalized with total EGFR in all three cell lines, either non-stimulated or stimulated with EGF, considering that Manders'

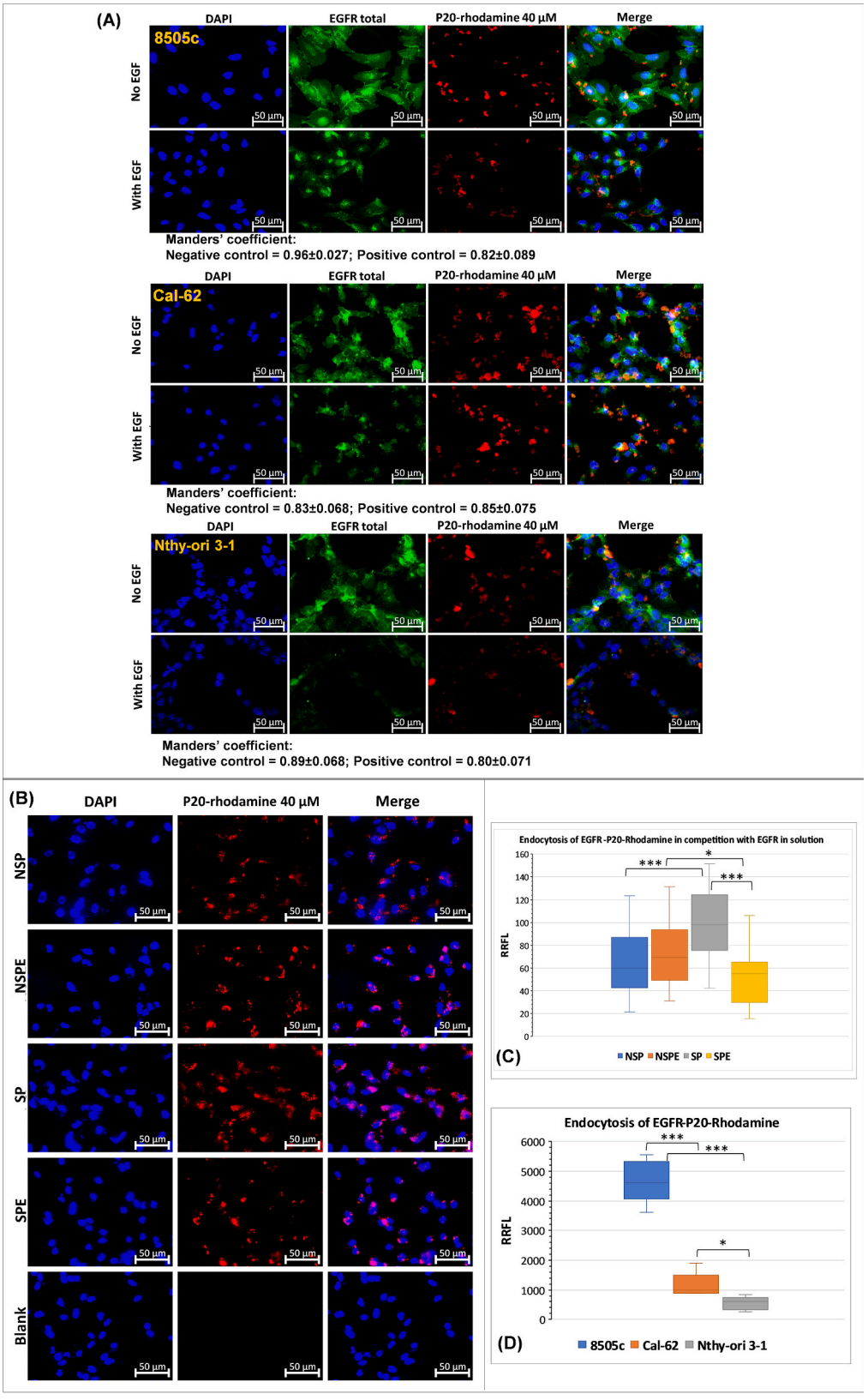

(caption on next page)

Fig. 4. Studies of P20-rhodamine endocytosis observed by IF on ATC cell lines 8505c and Cal-62 compared to healthy cell line Nthy-ori 3–1; the cells were either non-stimulated or stimulated with 1 μM EGF. (A) Colocalization of P20-rhodamine (stained in red) with total EGFR (stained in green) in 8505c, Cal-62 and Nthy-ori 3–1 cell lines (shown from up to down); nuclei are stained in blue with DAPI. The level of colocalization is expressed by the Manders' coefficient and the results are represented as means ± SD; n = 3/condition, 15 technical replicates. (B) Endocytosis of P20-rhodamine in competition with EGFR in solution within 8505c cells observed by fluorescence microscopy. NSP: non-stimulated cells incubated with P20-rhodamine; NSPE: non-stimulated cells incubated with P20-rhodamine and soluble EGFR; SP: cells stimulated with EGF and incubated with P20-rhodamine; SPE: cells stimulated with EGF and incubated with P20-rhodamine and soluble EGFR. (C) RRFL calculated for the results shown in panel B and expressed as percentage of SP; n = 5/condition, 25 technical replicates. (D) Endocytosis of P20-rhodamine in the three cell lines observed by IF expressed as RRFL normalized to the blank; n = 3/condition, 15 technical replicates. The results in C and D are presented in box-and-whisker plots where the statistical differences between experimental conditions were determined by the Mann-Whitney test. *: $p < 0.05$; ***: $p < 0.001$.

coefficient was ≥ 0.8 independently of EGF treatment. These results show that more than 80 % of P20 colocalizes with EGFR, which suggests that its endocytosis is carried out through the EGFR pathway. In microphotographs, P20-rhodamine (stained in red) generally appears as clusters in intracellular regions where EGFR (stained in green) is concentrated, probably within cellular compartments, including endocytosis vesicles and the nucleus (stained in blue).

According to literature, EGFR endocytosis is amplified in cancer cells due to its overexpression, being independent of EGF stimulation. The increased density of membrane EGFR causes spontaneous heterodimerization with ErBb2 in particular, which is responsible of an ineffective ubiquitination by the ubiquitin ligase Cbl E3, leading to EGFR recycling to the plasma membrane avoiding thus the lysosome degradation and pathway inactivation [42,43].

Our studies reported above suggested that P20 induced a decreased expression of total EGFR as well as of its phosphorylation, which may be related to the enhanced EGFR endocytosis triggered by P20. The subsequent studies aimed thus to elucidate some aspects of these processes.

3.7. P20 endocytosis in the presence of EGFR in solution

We then pursued our studies by preincubating P20-rhodamine with EGFR in solution (to allow their binding) before adding them to 8505c cells and observe peptide's endocytosis by IF. Four experimental conditions were investigated: (1) non-stimulated cells incubated with P20-rhodamine (NSP); (2) non-stimulated cells incubated with P20-rhodamine and soluble EGFR (NSPE); (3) cells stimulated with EGF and incubated with P20-rhodamine (SP); (4) cells stimulated with EGF and incubated with P20-rhodamine and soluble EGFR (SPE) (Figs. 4B and 4C).

No significant difference of P20 endocytosis could be observed between NSP and NSPE, which suggests that P20 is endocytosed by negative control cells despite its preincubation with soluble EGFR. However, a significantly decreased endocytosis has been observed in SPE compared to both SP ($p < 0.001$) and NSPE ($p < 0.05$), possibly implying that EGFR is already endocytosed due to EGF stimulation, which may limit its access to P20 binding and endocytosis. On the other hand, the significantly enhanced P20 endocytosis ($p < 0.001$) in SP compared to NSP suggests a cooperative effect between EGF and P20 on EGFR endocytosis. This phenomenon was also evoked by the results reported above (Fig. 3B), which suggested a decreased EGFR expression when both EGF and P20 were used to stimulate cells. Additionally, considering that stimulated cells were preincubated for 2 h with EGF but only SPE presented a significantly decreased P20 endocytosis compared to SP pleads for an EGFR-driven endocytosis; in this experimental condition, P20 was pre-incubated for 30 min with soluble EGFR, which prevented its EGFR-driven endocytosis.

Consequently, the integrated results of these studies lead to the hypothesis that EGF and P20 enhance together EGFR endocytosis through a cooperative effect, which implies that P20 follows the EGFR pathway of intracellular trafficking and probably contributes to its negative regulation.

In the framework of the same studies, we have compared the endocytosis of P20-rhodamine in the three cell types, which allowed us to conclude that cancer cells 8505c and Cal-62 present significantly higher levels of P20 uptake compared to Nthy-ori 3–1 cells, with the highest level being observed in 8505c cells (Fig. 4D). These results could be related to the higher EGFR expression in cancer cells (please see point 3.9. below) and are promising for an improved delivery of drugs in pathological conditions.

3.8. Total EGFR and P20 colocalization with endoplasmic reticulum, caveolae and nuclei

ER is part of the EGFR retrograde transport to the nucleus, contributing to its signaling network, whereas caveolae are an intracellular trafficking station leading to negative regulation of EGFR signaling by lysosomal degradation [6–10]. The goal of this study was thus to observe EGFR and P20 trafficking in ER, caveolae and nuclei by IF in 8505c cells non-treated or treated with EGF (Fig. 5A).

EGF induced an enhanced colocalization of total EGFR with ER (Manders' coefficient: 0.88, $p < 0.01$) and nuclei (Pearson coefficient: 0.39, $p < 0.01$) as compared to resting cells (Manders' coefficient: 0.69 in ER and Pearson coefficient: 0.31 in nuclei). These results are consistent with the literature considering that nuclear EGFR is often found in aggressive cancers [13].

The colocalization between the P20-TR and the ER was then studied to observe whether our peptide follows the same trafficking pathway as EGFR once endocytosed. The same as in the case of EGFR, EGF improved the colocalization of P20-TR with the ER (Manders' coefficient: 0.74, $p < 0.01$) and nuclei (Manders' coefficient: 0.76, $p < 0.01$) as compared to non-stimulated cells (Manders' coefficient: 0.58 in ER and Manders' coefficient: 0.53 in nuclei). However, these parameters reflect a much higher colocalization of P20-TR with ER and nuclei than for EGFR alone independently of EGF stimulation, suggesting that P20 promotes the intracellular trafficking of EGFR through the non-destruction pathway, resulting in its concentration within ER and nuclei, where many of EGFR signaling targets are located in cancer cells. The evasion of lysosomal destruction pathway by P20 is furthermore evoked by its decreased colocalization with caveolae in cells stimulated with EGF (Manders' coefficient: 0.038, $p < 0.001$) as compared to non-stimulated cells (Manders' coefficient: 0.13). EGFR degradation in lysosomes is preceded by its ubiquitination and caveolae internalization, which is known as "clathrin-independent pathway" [4,6,9].

To conclude, these results suggest that most of P20 follows the non-degradative EGFR intracellular trafficking pathway, leading to its accumulation in ER and nuclei, this phenomenon being promoted especially in EGF-stimulated cells.

3.9. Total and phosphorylated EGFR in cancer and control cell lines as determined by Western Blot

Our studies reported above suggested that EGFR is overexpressed and overactivated in cancer biopsies, as well as in 8505c and Cal-62 cell lines. Aiming to validate these results, we have determined by Western Blot the abondance of EGFR-pY1068 (Fig. 5B) and of total EGFR (Fig. 5C) in 8505c and Cal-62 cancer cell lines compared to healthy Nthy-ori 3–1 cell line. The effect of P20 on EGFR expression and phosphorylation was studied on cells stimulated or not with EGF, as explained above.

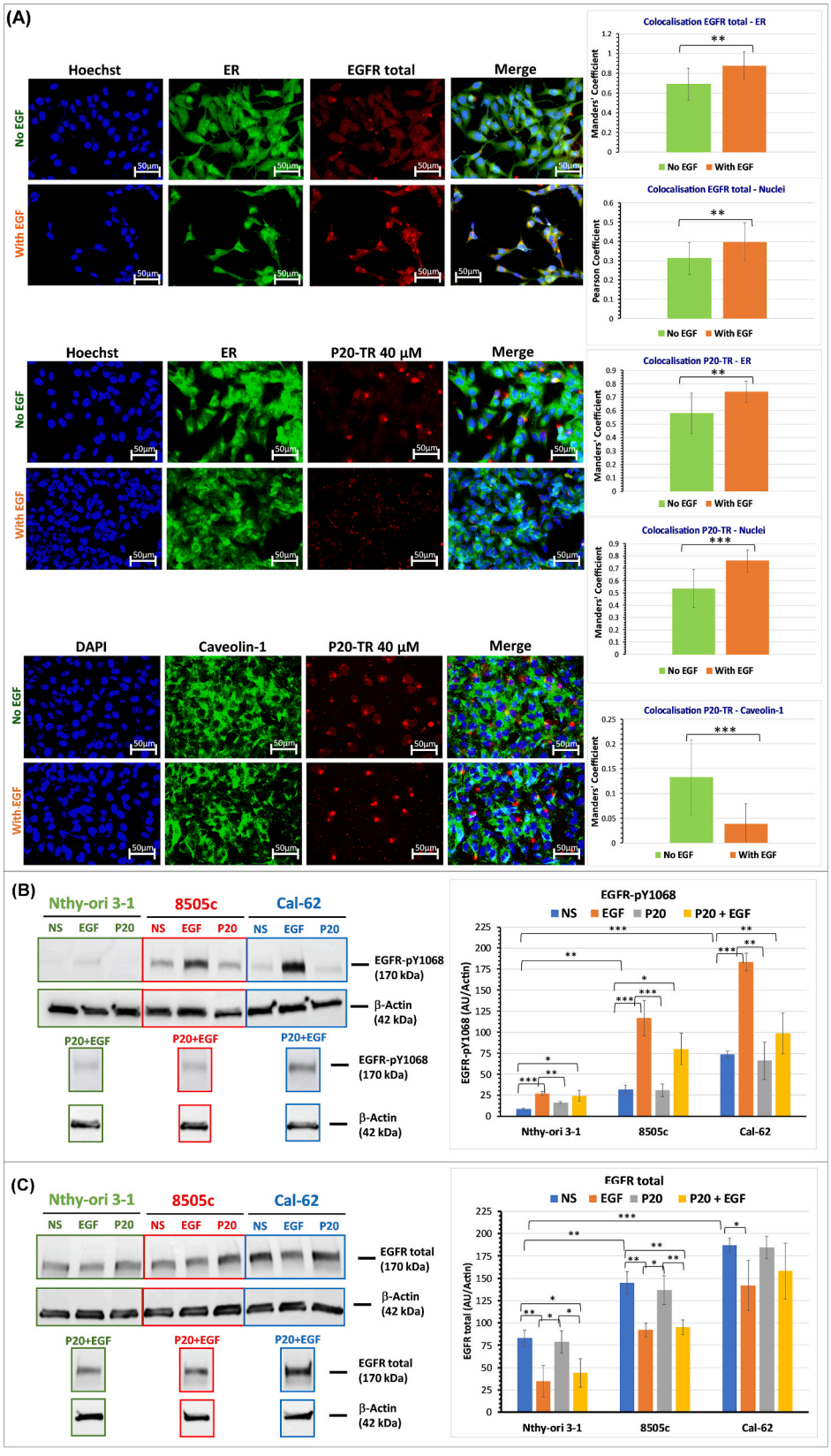

(caption on next page)

Fig. 5. Intracellular pathway of EGFR and of P20-TR observed by IF (studied on 8505c cell line) (A) and its effect on the cellular abundance of phosphorylated (B) and total (C) EGFR studied by Western Blot on Nthy-ori 3–1, 8505c and Cal-62 cell lines. The cells were either non-stimulated or stimulated with 1 μM EGF. In (A), the IF pictures representing the colocalization between total EGFR and ER (first panel) or between P20-TR and ER (second panel), nuclei (first and second panels) or caveolin-1 (third panel) are presented in left panels from up to down. The extent of colocalization is expressed by the Manders' or Pearson coefficients represented in the histograms shown on the right side of panel (A) [33]. Nuclei are stained with Hoechst (in the case of ER detection) or with DAPI (in the case of caveolae detection). **: $p < 0.01$; ***: $p < 0.001$; n = 3/condition, 15 technical replicates. Detection of EGFR-pY1068 (B) and of total EGFR (C) by Western Blot and the effect of P20 on EGFR abundance was carried out in n = 3–5 replicates per condition. Representative Western Blot images are shown on the left side of panels (B) and (C). Semiquantitative analysis of Western Blot results is represented in histograms presented on the right side of panels (B) and (C). NS stands for non-stimulated; *: $p < 0.05$; **: $p < 0.01$; ***: $p < 0.001$.

Cancer cells show an overactivation of EGFR compared to healthy cells, i.e., 3.69 and 8.52 times more EGFR-pY1068 was found in 8505c ($p < 0.01$) and Cal-62 ($p < 0.001$) cell lines, respectively, compared to the Nthy-ori 3–1 cell line (Fig. 5B). Secondly, one can notice that EGF induced the overactivation of EGFR in all cell lines compared to non-stimulated cells ($p < 0.001$) and those treated with P20 alone ($p < 0.01$; $p < 0.001$), which did not modify EGFR phosphorylation. On the other hand, P20 has the tendency to reduce EGFR phosphorylation although this effect remains statistically not significant. Our previous studies have shown that P20 is a non-competitive EGF antagonist inhibitor, which means that its effect on EGFR phosphorylation could be the consequence of the modification of EGFR conformation that would prevent EGF interaction with its binding sites.

Concerning total EGFR, cancer cells show an overexpression of EGFR, i.e. 1.74 and 2.25 times more total EGFR was found in 8505c ($p < 0.01$) and Cal-62 ($p < 0.001$) cell lines, respectively, compared to healthy cells (Nthy-ori 3–1) (Fig. 5C). EGF treatment induced in all cell lines a decreased amount of total EGFR compared to non-stimulated cells and to the cells treated with P20 alone (not statistically significant in Cal-62 cells); P20 alone or added to EGF-stimulated cells did not modify total EGFR abondance.

Aiming to understand how much of total EGFR is phosphorylated in cells treated with EGF and/or P20 and to hypothesize on its cellular pathway, we have estimated the percentage ratio of EGFRpY1068/total EGFR (Fig. 6Aa). This ratio confirms that cancer cell lines 8505c and Cal-62 present higher levels of EGFR phosphorylation both in EGF-stimulated ($p < 0.05$; $p < 0.005$) and non-stimulated cells ($p < 0.05$; 0.005). Moreover, EGF significantly enhanced EGFR phosphorylation in all cell lines, but especially in cancer cells. This ratio also corroborates the absence of P20′s effect on EGFR phosphorylation in cancer cells (but not in Nthy-ori 3–1 cells) when incubated with cells alone. On the other hand, P20 reduces EGFR phosphorylation in cancer cells ($p < 0.05$ in 8505c; $p < 0.01$ in Cal-62) stimulated with EGF (by 34 % and 52 % respectively) due to its role as a non-competitive EGF antagonist. Our studies allow us to hypothesize that this inhibitory effect of P20 could be the consequence of its binding to an allosteric site of EGFR combined with a stimulation of its endocytosis. The *trans*-autophosphorylation of Tyr residues located on the cytoplasmic tail of EGFR is possible only after its dimerization at the cell membrane. Therefore, it is possible that P20 blocks this dimerization and the subsequent EGFR phosphorylation. In Nthy-ori 3–1 cells, P20 decreased EGF-induced EGFR activation by 28 %, but the inhibitory effect did not reach statistical significance, probably due to the results' variability.

3.10. Effect of P20 on AKT signaling pathway and cell survival

Aiming to evaluate the effect of P20 on the activation and expression of AKT, the main component of the PAM signaling pathway activated by EGFR, we simultaneously assayed the total AKT and AKT phosphorylation at serine 473 (AKT-pSer473) or threonine 308 (AKT-pThr308) residues (Figs. 6Ab,c,d). PAM pathway is frequently activated in various human cancers, including ATC. AKT is a serine-threonine protein kinase often overexpressed in various cancers, where it plays a key role in cell survival, growth, and proliferation [44].

Our results show an overexpression of total AKT in the Cal-62 ATC cell line ($p < 0.05$) and an overactivation via Thr308 phosphorylation in 8505c cell line ($p = 0.05$) as compared to Nthy-ori 3–1 cell line.

P20 did not produce any significant effect on total AKT expression (Fig. 6Ab) in any of the three cell lines. On the other hand, P20 enhanced significantly ($p < 0.001$) the phosphorylation of AKT at Ser473 in Nthy-ori 3–1 cells (Fig. 6Ac), which might be related to its stimulating effect on EGFR phosphorylation ($p < 0.01$) in the same cell line (Fig. 6Aa), suggesting the activation of the pathways involved in cell survival and growth.

Contrarywise, P20 induced a significant decrease ($p < 0.05$) of AKT-Ser473 phosphorylation in 8505c cells (Fig. 6Ac), as well as of AKT-Thr308 ($p < 0.05$) in 8505c and Cal-62 cell lines (Fig. 6Ad), probably explained by the peptide's effect as a non-competitive inhibitor of EGFR, which prevents the activation of downstream signaling pathways, including those governed by AKT.

AKT is a key proto-oncogene involved in the process of cell survival by inhibitory phosphorylation of the pro-apoptotic protein Bad on its Ser136 residue [44]. We have thus investigated the effect exerted by P20 on Bad expression (total Bad) and phosphorylation (Bad-pSer136) (Figs. 6Ba,b,c) through EGFR/AKT signaling pathway.

8505c ($p < 0.05$) and Cal-62 ($p < 0.01$) cell lines present a significantly lower abundance of Bad-pSer136/Bad-Total (Figs. 6Bb,c) compared to Nthy-ori 3–1 cells (Fig. 6Ba), which corroborates scientific literature showing a decreased activity of pro-apoptotic proteins like Bad in several cancer types, such as breast, ovarian and lung cancers [45]. On the other hand, treatment of cells with P20 did not cause any statistically significant effects on any cell line, which is rather reassuring because this peptide was selected with the aim of acting as a vector in the targeted delivery of therapeutic or diagnostic agents. Moreover, our results confirmed that P20 does not modify significantly cell viability, which remains around 90 % independently of experimental conditions and cell line (Figs. 6Ca,b,c).

Globally, our studies confirmed that P20 acts as a non-competitive inhibitor of EGFR in cancer cells, which explains its inhibitory effect on AKT phosphorylation, although this activity does not affect cell survival, probably due to the triggering of other counteracting signaling pathways.

3.11. Evaluation of eventual in vivo toxicity effects of P20

In order to propose P20 as a vector peptide for diagnostic or therapeutic agents, its potential toxic effects were evaluated on NMRI mice treated for 3 weeks (3 times per week) with 200 nmol/kg b.w. of P20 (assessment group). This dose and duration of treatment were chosen based on our studies performed with P20 covalently coupled to a pharmacological compound capable of treating ATC in a murine model; these studies will be the subject of a separate publication. In that study, P20 was administered at a dose of 10 nmol/kg for 2–3 weeks (3 times per week). In the present work, we arbitrarily decided to enhance this dose 20-fold. Negative control animals were treated with 0.9 % NaCl. The weight of mice was measured before each treatment and before the sacrifice and the results are presented in Fig. 7A. At the end of the treatment period, clinical biochemistry parameters (ALT, AST, T-Chol, T-Bil, BUN and glucose) were measured in blood plasma (Table 2) whereas apoptosis was detected in liver by IF staining of activated caspase-3 (Fig. 7**B-E**). Healthy and apoptotic livers obtained in our previous studies were used as negative and positive controls,

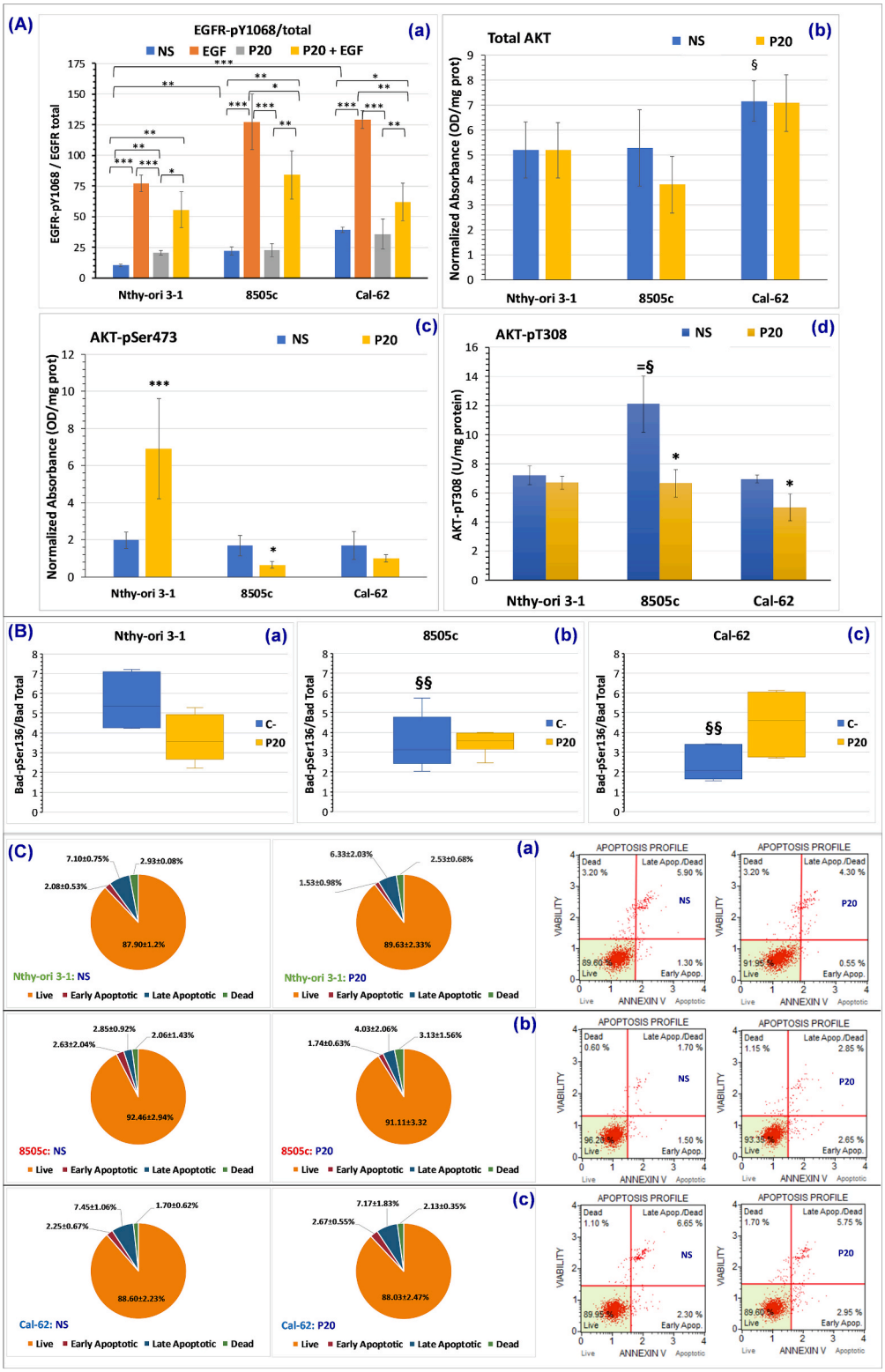

Fig. 6. Effect of P20 on EGFR phosphorylation, AKT signaling pathway and cell survival, studied in Nthy-ori 3–1, 8505c and Cal-62 cell lines; the cells were either non-stimulated (NS) or stimulated with 1 μM EGF. (A) The first histogram (in (a), left corner, up) shows the ratio of EGFR-pY1068 over total EGFR obtained by Western Blot as explained in Fig. 5. The three other histograms show the level of total AKT (in (b), right corner, up), as well as that of AKT-pSer473 (c) (n = 3–6 per condition) and of AKT-pThr308 (d) (n = 3–4 per condition) (second row). In AKT histograms, *: $p < 0.05$ and ***: $p < 0.001$ are compared to corresponding non-stimulated cells. (B) Rate of activation of the Bad protein, expressed as the ratio of Bad-pSer136 to the total amount of Bad and represented in box-and-whisker plots (n = 3–7 per condition) Nthy-ori 3–1 (a), 8505c (b) and Cal-62 (c) cell lines. (Ca,b,c) Effect of P20 on cell survival, detected by flow cytometry using Annexin V and 7-AAD shown in pie charts (on the left side) and in representative flow cytometry charts (on the right side) (n = 3 per condition); (a) shows Nthy-ori 3–1 cell line, (b) shows 8505c cell line, (c) shows Cal-62 cell line. *: $p < 0.05$; **: $p < 0.01$; ***: $p < 0.001$; =§: $p = 0.05$; §: $p < 0.05$; §§: $p < 0.01$ for 8505c or Cal-62 vs. Nthy-ori 3–1.

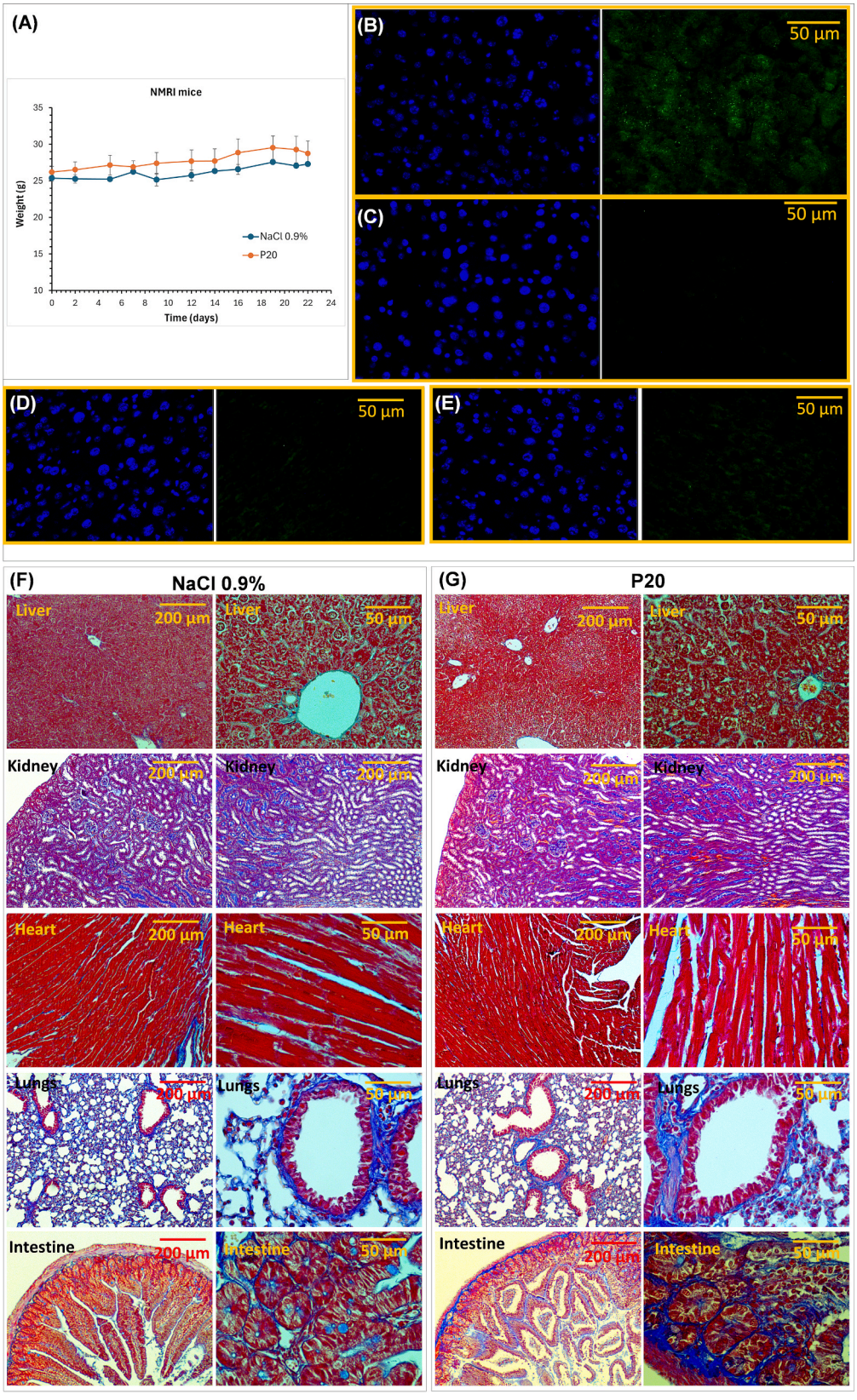

Fig. 7. Studies of toxicity carried out *in vivo* on NMRI mice treated for 3 weeks (3 times per week) either with 0.9 % NaCl (negative control group) or with P20 (assessment group). (A) The weight of mice measured during the treatment period. (B) Apoptotic liver obtained as described in [46]. (C) Healthy control liver obtained as described in [47]. (D) Activated caspase-3 detection in P20-treated mouse. (E) Activated caspase-3 detection in 0.9 % NaCl-treated mouse. Pictures of fluorescence microscopy shown in B-E present nuclei stained in blue with DAPI and the corresponding green staining (Dylight 488) of activated caspase-3. (F and G) Histological sections of organs collected from mice treated with 0.9 % NaCl (F) or with P20 (G) and stained with Masson's Trichrome.

Table 2
Clinical biochemistry parameters measured in blood plasma of NMRI mice treated either with 0.9% NaCl (control group) or with P20 (assessment group). No statistical differences could be identified between experimental groups.

Parameter (reference values cited from [48])	Experimental groups (means ± SD)	
	0.9 % NaCl	P20
Glucose (mg/dL) (228.2; range 146.2–273.6)	442.63 ± 95.51	355.55 ± 16.32
Cholesterol (mg/dL) (99.38; range 85.46–106.73)	116.8 ± 7.05	125.60 ± 16.11
BUN (mg/dL) NA	34.14 ± 3.19	32.57 ± 6.79
T-Bil (mg/dl) NA	0.71 ± 0.22	0.43 ± 0.13
AST (IU/L) (107.21; range 80–160)	210.79 ± 56.83	119.07 ± 47.01
ALT (IU/L) (44; range 24–89)	66.54 ± 23.47	25.59 ± 8.63

Note: NA = not available.

respectively [46,47]. The morphology of various organs (liver, kidneys, heart, lungs, intestine) was observed by microscopy on histological sections stained by Masson's Trichrome technique (Fig. 7**F-G**).

No signs of distress were noted in the mice during the treatment period, regardless of the anesthesia or type of treatment received, suggesting that neither P20 nor 0.9 % NaCl administration induced any visible side effects. Regarding the weight of animals, no statistically significant differences were observed between groups ($p > 0.05$) (Fig. 7A), suggesting that P20 did not have an impact on this parameter compared to the control group.

The Masson's Trichrome staining of livers (Fig. 7**F-G**) revealed that some hepatocytes present clear and vacuolate cytoplasm, regardless of the experimental group. However, these observations could be attributed to normal glycogen accumulation in hepatocytes characteristic to rodents. Apart from this aspect, no evidence of liver damage was observed by this method. Blood transaminases (Table 2) present slightly higher values of AST and ALT in the group treated with 0.9 % NaCl compared to reference values, but no statistical differences could be identified compared to P20-treated group. Hyperglycemia (especially in 0.9 % NaCl treated group) and hypercholesterolemia observed in both experimental groups compared to reference values (Table 2) could be related to *ad libitum* access of animals to food intake, although they may be partly explained by a metabolic distress related to hepatic disfunction. T-Bil in humans (values not available for NMRI mice) ranges from 0.2 to 1 mg/dL, which suggests that no major liver lesion was induced by any of the applied treatments since T-Bil remains within this range. Aiming to identify more precisely eventual liver lesions, we have determined the presence of activated caspase-3 by IF on liver sections (Fig. 7**B-E**). A mild apoptosis was observed especially in the livers of control mice and lower in those of P20-treated mice, which was probably induced by isoflurane and ketamine, as described in literature [49,50]. These results therefore indicate that the P20 treatment did not cause liver toxicity.

The kidneys exhibit normal morphology in both groups of mice (Fig. 7**F-G**). However, an elevated blood BUN level was observed in both experimental groups (Table 2) compared to human reference values (8–20 mg/dL), which could be explained by protein breakdown rather than by kidney dysfunction. Since the two groups of mice have similar results, it can be concluded that P20 does not induce toxicity in the kidneys.

P20 or 0.9 % NaCl did not induce any significant morphological modifications of hearts and intestines either, since no evidence of injury or fibrosis was detected (Fig. 7**F-G**) on histological sections stained by Masson's Trichrome technique. These results suggest that treatment with P20 does not induce cardiac and intestinal toxicity.

In the case of lungs, many pink or red cells were observed in the capillaries adjacent to the alveoli (Fig. 7**F-G**), raising questions about the possibility of leukocyte infiltration. In order to address this question, IHC staining of IL-7R was performed on lung sections (data not shown) as described before [51]. This receptor is expressed by various immune cells, e.g., T cells, B cell precursors, bone marrow macrophages [52]. The absence of IL-7R immunostaining confirmed that cellular infiltration in the lungs of both experimental groups are not leukocytes, suggesting that no inflammatory infiltration was produced by the applied treatment. This reinforces the idea that anesthetic compounds could be responsible for blood cell infiltration in the lungs, considering that isoflurane and ketamine are known as systemic vasodilators, which may have caused a greater blood flow to the lung capillaries.

To conclude, these results indicate that P20 did not cause any toxic events in NMRI mice in our experimental conditions, considering that no significant difference could be observed compared to 0.9 % NaCl-treated mice. The morphological and biochemical abnormalities associated with liver and lung tissues are explained by long-term administration of anesthetics as described by literature.

3.12. P20 homing to 8505c ATC tumors studied by FLI

Aiming to assess the ability of P20 to deliver a pharmacological moiety to ATC tumors, the peptide was covalently coupled to an optical imaging probe, namely IRDye800 (IRDye800-P20), and observed by FLI in athymic nude mice bearing 8505c tumors (Fig. 8A). The specific targeting of EGFR by IRDye800-P20 was investigated by an *in vivo* competition experiment, where the imaging probe (1.2 μmol/kg b.w.) was preceded by the free P20 (2.4 μmol/kg b.w.) injected 10 min before IRDye800-P20 (Fig. 8B). A pilot feasibility FLI study allowed us to select the optimal dose of IRDye800-P20 after assessing 0.4 μmol/kg b.w., 0.8 μmol/kg b.w. and 1.2 μmol/kg b.w..

Images were acquired before (pre-dye) and 30, 60 and 120 min after the injection of IRDye800-P20 and the signal intensity (SI) of tumors was measured and expressed as the ratio post-dye/pre-dye (Fig. 9A, left graph). Moreover, the SI measured post-dye on tumors was normalized to SI measured on contralateral thigh in the absence and in the presence of the P20 competitor to better reflect the effect produced by the competition experiment (Fig. 9A, right graph). The tumors were collected from mice at the end of FLI studies, and total EGFR and EGFR-pY1068 were detected by IHC to confirm the receptor expression and activation.

The maximum signal is attained in tumors 30 min after IRDye800-P20 administration (SI of 468 ± 26 in the absence of free P20 vs. 368 ± 34 in the presence of free P20) and decreases progressively in both experimental groups due to renal excretion, attaining a minimum 120 min after administration (124 ± 43 in the absence of free P20 vs. 86 ± 23 in the presence of free P20) (Figs. 8A and 9A, left graph). The SI measured in tumors is inferior in the presence of the competitor, attesting for the partial displacement of the imaging probe from the targeted EGFR sites by the free P20 already bound and present in higher concentration (Figs. 8B and 9A, left graph).

The percentage difference of tumor's SI compared to the contralateral thigh (considered as a non-targeted negative control) attained a maximum of 21.2 % 120 min after IRDye800-P20 administration, when the specific contrast was the highest, likely due to the EGFR binding in tumors (Fig. 9A, right graph). In the mice subjected to free P20 competition, the same parameter varied from −13.05 ± 7.25 at 30 min post-dye to −0.35 ± 8.89 at 120 min post-dye, revealing that the contralateral SI was higher than or relatively equal to the SI measured in tumors. This is explained by EGFR binding in tumors by the free P20, which limited IRDye800-P20 access to the target as explained above, attesting for the specific targeting of this receptor in tumors, where its expression is approximately 2 times higher both in ATC tumor biopsies (Figs. 3**D,E**) and in cell lines (Figs. 5**B,C**).

EGFR expression and activation was furthermore confirmed in 8505c tumors collected from mice after FLI studies (Figs. 9**B,C,D**). Total EGFR

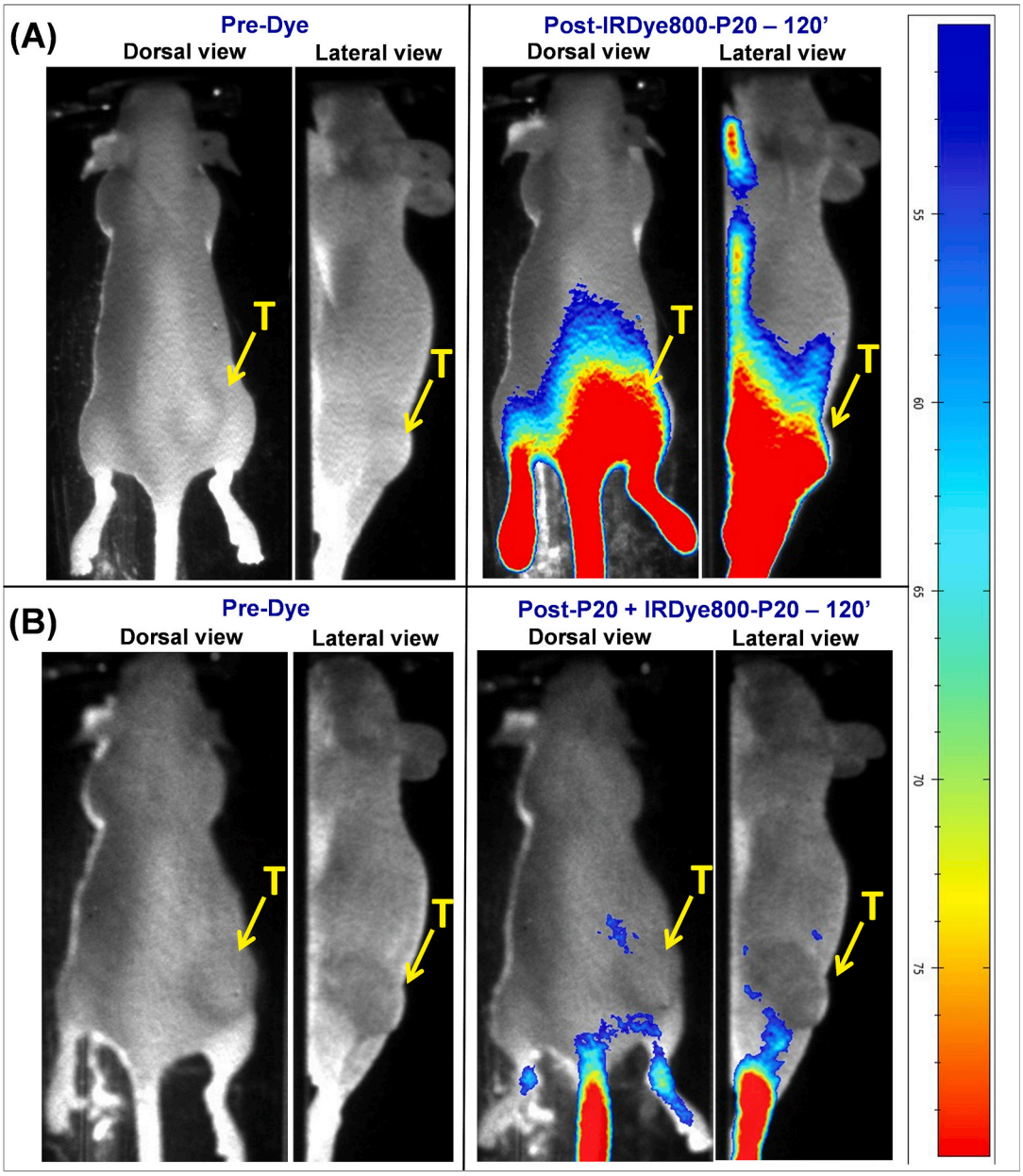

Fig. 8. FLI images of athymic nude mice bearing 8505c tumors acquired before (Pre-Dye) and 120 min after the injection of IRDye800-P20 (Post-IRDye800-P20) in the absence (n = 3) (A) and in the presence of the P20 competitor (n = 4) (B) injected 10 min before the imaging probe.

includes both phosphorylated and non-phosphorylated receptors (Fig. 9B) and is observed partly at the membrane level, and more often in the cytoplasm and quite rarely in the nuclei, corresponding to its characteristic cellular distribution. EGFRpY1068 is much more concentrated at the membrane level, where EGFR is activated by its ligands, although it can also be observed in the cytoplasm (probably within organelles like ER and Golgi apparatus) and more scarcely in the nuclei, due to its retrograde intracellular traffic as explained above (Fig. 9C). The EGFR fraction localized at the cell membrane level is the one that is exploitable for the targeted delivery of diagnostic and therapeutic agents, and the possibility to be endocytosed is a condition for an optimal release of therapeutic moieties within cells.

The semi-quantitative analysis of EGFR immunostaining in tumors by ImageJ (Fig. 9D) shows that this biomarker is heterogeneously expressed within 8505c tumors, with values that range between 18.6 % and 69.8 % for total EGFR and between 10 % and 67.9 % for EGFRpY1068.

Altogether, these results reveal that P20 is specifically concentrated in 8505c tumors, likely due to its binding to EGFR exposed by cancer cells at the membrane level especially in a phosphorylated state.

4. Discussion and conclusions

Although rare, the ATC is an aggressive and invasive type of TC, with a dismal prognosis, presenting a median survival rate of 2-6 months after diagnosis. The standard treatment consists of combining surgery with ionizing radiation and chemotherapy. However, chemotherapeutic agents are administered systemically producing many side effects, whereas ATC becomes resistant to standard therapies. Therefore, a fundamental change in the therapeutic strategy's conception is required to manage this life-threating oncologic disease.

In this context, the goal of the present work was to develop a vector molecule able to assist the EGFR-mediated drug delivery to ATC cells, while sparing healthy cells as much as possible. EGFR was chosen

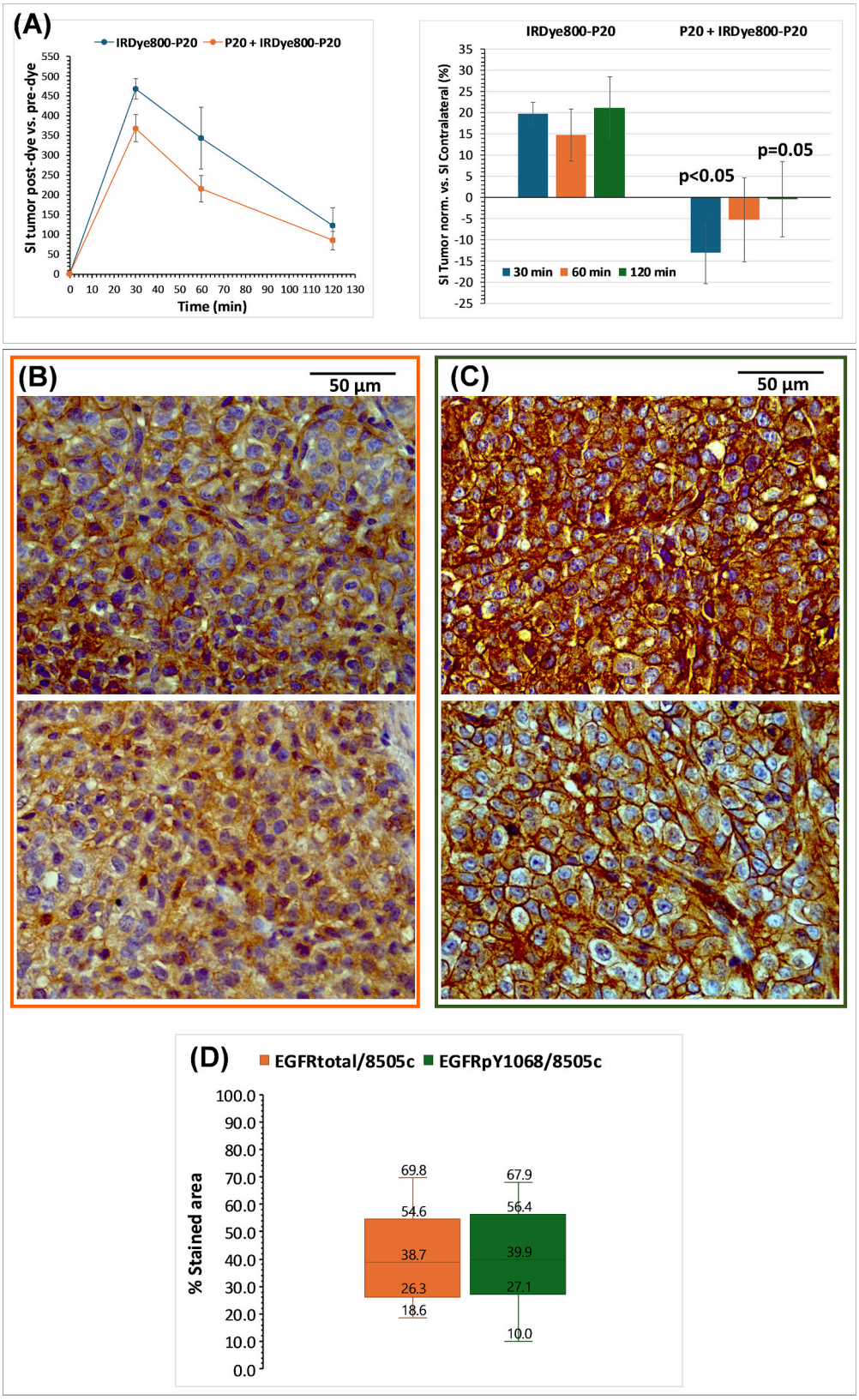

Fig. 9. Signal intensity (SI) measurement on FLI images of tumors (shown in Fig. 8) and detection of EGFR in 8505c tumors by immunohistochemistry after FLI studies. (A) SI of tumors measured post-dye is normalized to SI measured pre-dye (left graph); SI measured post-dye on tumors is normalized to contralateral thigh (percentage difference of SI in tumors vs. contralateral thigh) in the absence and in the presence of the P20 competitor (right graph). Total EGFR (B) and EGFR-pY1068 (C) were stained by IHC on 8505c tumors collected from mice after FLI studies. EGFR immunostaining was semi-quantitatively determined by ImageJ and the percentage of stained area was represented graphically in Figure shown in (D).

because it is overexpressed in many cancers including ATC and it is internalized, which ultimately allows the drug to be delivered directly into cancer cells. To attain this objective, vector peptides targeting the EGFR were searched by phage display, peptide P20 being identified as the most promising candidate.

The molecular mechanism of P20 binding to EGFR has been analyzed *in silico* by peptide-protein docking studies using the HPEPDOCK web server. P20 has a theoretical half-life of 100 h and binds to the interface between domains I and III of EGFR, in the large hydrophobic pocket exposing the binding sites to EGF. Altogether, our results reveal that P20 presents the optimal characteristics for EGFR-targeted drug delivery based on the following arguments: (1) P20 targets EGFR overexpressed by cancer cells and discriminates between healthy and tumor cells; (2) it induces EGFR endocytosis without activating it and without interfering with EGF binding; (3) P20 is a non-competitive inhibitor of EGFR and follows the non-degradative EGFR intracellular pathway; (4) it may contribute to the therapeutic effect of an anti-cancer drug by decreasing the expression and activation of EGFR, as well as of AKT phosphorylation in ATC cells; (5) P20 does not induce toxic effects *in vivo* in the main tissues and organs; (6) it is concentrated in tumors, where the peptide is retained for longer time than in other tissues due to its specific binding to EGFR.

The next objective of our project is dedicated to the conception and characterization of an innovative pharmacological formulation combining P20 to a therapeutic moiety comprising a peptide capable of inducing ATC cell apoptosis by blocking the PAM pathway. Bioactive peptides are at the cutting edge of the contemporary search for novel, potent, selective and safe therapeutic agents [53,54]. In the case of anticancer therapies targeting EGFR, antibodies specific to the extracellular ligand-binding domain of EGFR or various quinazoline derivatives targeted to the intracellular TK domain of EGFR have been largely used to block receptor activation [13]. For specific delivery of therapeutic agents to cancer cells, it is crucial to target ED-EGFR, as it is exposed on the cell surface and is therefore accessible to vectoring agents [7]. Although many antibodies targeting ED-EGFR have already been developed, they present several limitations compared to peptides, notably higher immunogenicity, susceptibility to endogenous proteolysis and production costs, more complex chemical derivatization, and challenging *in silico* selection and chemical optimization [54]. Based on these pharmacological concepts and limitations, we focused our attention on the development of novel peptide-based ATC therapeutic strategies.

It is worth noting that a wide range of genetic alterations have been identified in ATC, covering both oncogenes (such as *BRAF*, *NRAS*, *KRAS*, *HRAS*) and tumor suppressor genes (such as *TP53*, *NF1*, *PTEN*) [55,56]. These alterations result in the activation of major signaling pathways, including MAPK and PAM, which promote proliferation, cell survival, and resistance to conventional treatments [27]. Therapies targeting these pathways have been developed, such as inhibitors of BRAF (dabrafenib, vemurafenib), MEK (trametinib), mTOR (everolimus), as well as multi-target inhibitors such as lenvatinib or sorafenib, which have shown promising results, particularly in combination [57,58]. At the same time, new strategies, such as immunotherapy (anti-PD-1 antibodies) or inhibitors of new targets (Aurora kinases, HDACs, β-catenin), are integrated in clinical trials. These combined approaches aim to circumvent resistance mechanisms and strengthen the antitumor response. Several randomized trials are underway to validate the effectiveness of these combinations in ATC, with the aim of improving the still poor prognosis of this pathology [59,60]. A novel strategy of targeted drug delivery has also been proposed by combining an aptamer targeting CD133, a glycoprotein specifically expressed in ATC, with doxorubicin, a cytotoxic agent from the anthracycline class [61].

Nevertheless, a potential limitation of the targeted therapy in cancer is the heterogenous expression of specific biomarkers within the same tumor, both spatially and temporarily, and the multiple resistance mechanisms triggered by cancer cells after chronic treatment.

CRediT authorship contribution statement

Zehra-Cagla Kahvecioglu: Writing – original draft, Validation, Methodology, Investigation, Formal analysis, Conceptualization. **Samuel Vandecasteele:** Writing – original draft, Validation, Methodology, Investigation, Formal analysis. **Marine Bougard:** Writing – original draft, Validation, Methodology, Investigation, Formal analysis. **Olivia Rasson:** Writing – original draft, Validation, Methodology, Investigation, Formal analysis. **Amandine Nachtergael:** Writing – review & editing, Visualization, Validation, Formal analysis, Conceptualization. **Pierre Duez:** Writing – review & editing, Visualization, Supervision, Formal analysis, Conceptualization. **Denis Nonclercq:** Writing – review & editing, Visualization, Validation, Supervision, Formal analysis. **Myriam Remmelink:** Writing – review & editing, Visualization, Validation, Supervision, Formal analysis. **Sophie Laurent:** Writing – review & editing, Visualization, Validation, Supervision, Resources, Project administration, Funding acquisition, Formal analysis, Conceptualization. **Sven Saussez:** Writing – review & editing, Visualization, Supervision, Resources, Project administration, Funding acquisition, Formal analysis, Conceptualization. **Carmen Burtea:** Writing – review & editing, Writing – original draft, Visualization, Validation, Supervision, Resources, Project administration, Methodology, Investigation, Funding acquisition, Formal analysis, Data curation, Conceptualization.

Declaration of competing interest

The authors declare that they have no known competing financial interests or personal relationships that could have appeared to influence the work reported in this paper.

Acknowledgements

This work was funded by the ARC (*Actions de Recherche Concertée*) Programs (2014 – 2019 and 2024 – 2029) of the Wallonia-Brussels Federation, the Télévie-FNRS (*Fonds National de la Recherche Scientifique*) grant (2020 – 2025) and the FRMH (*Fond pour la Recherche Médicale en Hainaut)* grants, all from Belgium. The authors thank Dr. Lionel Larbanoix and Ms. Justine Allard from the Center for Microscopy and Molecular Imaging (supported by the European Regional Development Fund, European Union, and the Wallonia-Brussels Federation, Belgium) for the *in vivo* studies performed by Fluorescence Imaging and the histological processing of the organ and tissue samples. Drs. Isabelle Salmon, Sandrine Rorive and Lara Absil (Department of Pathology, Erasme Hospital, ULB, Brussels, Belgium) are thanked for the provided ATC and healthy human biopsy sections. Professor Lionel Tafforeau (Faculty of Sciences, UMONS, Belgium) is acknowledged for the access to the Western Blot Imager (Bioimager Fusion FX) purchased through a fund granted by FNRS, Belgium. Bachelor and Master students, Sarah Peeters, Manon Bruynbroeck, Danièle Feudjio Tagni and Ami Toulehohoun are thanked for their contribution to this study.

Data availability

Data will be made available on request.

References

[1] M.A. Lemmon, J. Schlessinger, K.M. Ferguson, The EGFR Family: not so prototypical receptor tyrosine kinases, Cold Spring Harb. Perspect. Biol. 6 (4) (2014) a020768, https://doi.org/10.1101/cshperspect.a020768.

[2] N. Normanno, A. De Luca, C. Bianco, L. Strizzi, M. Mancino, M.R. Maiello, A. Carotenuto, G. De Feo, F. Caponigro, D.S. Salomon, Epidermal growth factor receptor (EGFR) signaling in cancer, Gene 366 (1) (2006) 2–16, https://doi.org/10.1016/j.gene.2005.10.018.

[3] T. Amelia, R.E. Kartasasmita, T. Ohwada, D.H. Tjahjono, Structural insight and development of EGFR tyrosine kinase inhibitors, Molecules 27 (3) (2022) 819, https://doi.org/10.3390/molecules27030819.

[4] A. Conte, S. Sigismund, Chapter Six - The ubiquitin network in the control of EGFR endocytosis and signaling, in: S.K. Shenoy (Ed.), Prog. Mol. Biol. Transl. Sci., vol. 141, Ubiquitination and Transmembrane Signaling, Academic Press, 2016, pp. 225–276, https://doi.org/10.1016/bs.pmbts.2016.03.002.

[5] R. Zandi, A.B. Larsen, P. Andersen, M.T. Stockhausen, H.S. Poulsen, Mechanisms for oncogenic activation of the epidermal growth factor receptor, Cell. Signal. 19 (10) (2007) 2013–2023, https://doi.org/10.1016/j.cellsig.2007.06.023.

[6] A. Tomas, C.E. Futter, E.R. Eden, EGF receptor trafficking: consequences for signaling and cancer, Trends Cell Biol. 24 (1) (2014) 26–34, https://doi.org/10.1016/j.tcb.2013.11.002.

[7] A.A. Rosenkranz, T.A. Slastnikova, Epidermal growth factor receptor: Key to selective intracellular delivery, Biochemistry (Mosc.) 85 (9) (2020) 967–993, https://doi.org/10.1134/S0006297920090011.

[8] Y.N. Wang, H. Yamaguchi, J.M. Hsu, M.C. Hung, Nuclear trafficking of the epidermal growth factor receptor family membrane proteins, Oncogene 29 (28) (2010) 3997–4006, https://doi.org/10.1038/onc.2010.157.

[9] I. Pinilla-Macua, A. Sorkin, Methods to study endocytic trafficking of the EGF receptor, Methods Cell Biol. 130 (2015) 347–367, https://doi.org/10.1016/bs.mcb.2015.05.008.

[10] T. Tanaka, Y. Zhou, T. Ozawa, R. Okizono, A. Banba, T. Yamamura, E. Oga, A. Muraguchi, H. Sakurai, Ligand-activated epidermal growth factor receptor (EGFR) signaling governs endocytic trafficking of unliganded receptor monomers by non-canonical phosphorylation, J. Biol. Chem. 293 (7) (2018) 2288–2301, https://doi.org/10.1074/jbc.M117.811299.

[11] T.M. Brand, M. Iida, N. Luthar, M.M. Starr, E.J. Huppert, D.L. Wheeler, Nuclear EGFR as a molecular target in cancer, Radiother. Oncol. 108 (3) (2013) 370–377, https://doi.org/10.1016/j.radonc.2013.06.010.

[12] M.K. Chen, M.C. Hung, Proteolytic cleavage, trafficking, and functions of nuclear receptor tyrosine kinases, FEBS J. 282 (19) (2015) 3693–3721, https://doi.org/10.1111/febs.13342.

[13] B. Atwell, P. Chalasani, J. Schroeder, Nuclear epidermal growth factor receptor as a therapeutic target, Explor. Target Antitumor Ther. 4 (4) (2023) 616–629, https://doi.org/10.37349/etat.2023.00156.

[14] D. Sabbah, R. Hajjo, K. Sweidan, Review on epidermal growth factor receptor (EGFR) structure, signaling pathways, interactions, and recent updates of EGFR inhibitors, Curr. Top. Med. Chem. 20 (2020), https://doi.org/10.2174/1568026620666200303123102.

[15] H. Lote, J. Bhosle, K. Thway, K. Newbold, M. O'Brien, Epidermal growth factor mutation as a diagnostic and therapeutic target in metastatic poorly differentiated thyroid carcinoma: a case report and review of the literature, Case Rep, Oncol 7 (2014) 393–400, https://doi.org/10.1159/000364856.

[16] B.A. Schiff, A.B. McMurphy, S.A. Jasser, M.N. Younes, D. Doan, O.G. Yigitbasi, S. Kim, G. Zhou, M. Mandal, B.N. Bekele, F.C. Holsinger, S.I. Sherman, S.C. Yeung, A.K. El-Naggar, J.N. Myers, Epidermal growth factor receptor (EGFR) is overexpressed in anaplastic thyroid cancer, and the EGFR inhibitor gefitinib inhibits the growth of anaplastic thyroid cancer, Clin. Cancer Res. 10 (24) (2004) 8594–8602, https://doi.org/10.1158/1078-0432.CCR-04-0690.

[17] H.K. Gan, A.N. Cvrljevic, T.G. Johns, The epidermal growth factor receptor variant III (EGFRvIII): where wild things are altered, FEBS J. 280 (21) (2013) 5350–5370, https://doi.org/10.1111/febs.12393.

[18] M.V. Grandal, R. Zandi, M.W. Pedersen, B.M. Willumsen, B. van Deurs, H. S. Poulsen, EGFRvIII escapes down-regulation due to impaired internalization and sorting to lysosomes, Carcinogenesis 28 (7) (2007) 1408–1417, https://doi.org/10.1093/carcin/bgm058.

[19] J. Capdevila, A. Awada, D. Führer-Sakel, S. Leboulleux, P. Pauwels, Molecular diagnosis and targeted treatment of advanced follicular cell-derived thyroid cancer in the precision medicine era, Cancer Treat. Rev. 106 (2022) 102380, https://doi.org/10.1016/j.ctrv.2022.102380.

[20] Z. Li, Y. Zhang, R. Wang, K. Zou, L. Zou, Genetic alterations in anaplastic thyroid carcinoma and targeted therapies, Exp. Ther. Med. 18 (4) (2019) 2369–2377, https://doi.org/10.3892/etm.2019.7869.

[21] M.E. Cabanillas, D.G. McFadden, C. Durante, Thyroid cancer, Lancet 388 (10061) (2016) 2783–2795, https://doi.org/10.1016/S0140-6736(16)30172-6.

[22] A. Prete, P. Borges de Souza, S. Censi, M. Muzza, N. Nucci, M. Sponziello, Update on fundamental mechanisms of thyroid cancer, Front. Endocrinol. 11 (2020) 102, https://doi.org/10.3389/fendo.2020.00102.

[23] F. Limaiem, S. Kashyap, P.T. Naing, A.O. Giwa, Anaplastic thyroid cancer, in: StatPearls, Treasure Island (FL), StatPearls Publishing, 2023. http://www.ncbi.nlm.nih.gov/books/NBK538179/.

[24] A.K. Abe, Lam, Anaplastic thyroid carcinoma: current issues in genomics and therapeutics, Curr. Oncol. Rep. 23 (3) (2021) 31, https://doi.org/10.1007/s11912-021-01019-9.

[25] E. Molinaro, C. Romei, A. Biagini, E. Sabini, L. Agate, S. Mazzeo, G. Materazzi, S. Sellari-Franceschini, A. Ribechini, L. Torregrossa, F. Basolo, P. Vitti, R. Elisei, Anaplastic thyroid carcinoma: from clinicopathology to genetics and advanced therapies, Nat. Rev. Endocrinol. 13 (11) (2017) 644–660, https://doi.org/10.1038/nrendo.2017.76.

[26] W.A. Lai, C.Y. Liu, S.Y. Lin, C.C. Chen, J.F. Hang, Characterization of driver mutations in anaplastic thyroid carcinoma identifies RAS and PIK3CA mutations as negative survival predictors, Cancers (Basel) 12 (7) (2020) 1973, https://doi.org/10.3390/cancers12071973.

[27] D. Laha, N. Nilubol, M. Boufraqech, New therapies for advanced thyroid cancer, Front. Endocrinol. 11 (2020) 82, https://doi.org/10.3389/fendo.2020.00082.

[28] S. De Leo, M. Trevisan, L. Fugazzola, Recent advances in the management of anaplastic thyroid cancer, Thyroid Res. 13 (1) (2020) 17, https://doi.org/10.1186/s13044-020-00091-w.

[29] D. Fanfone, N. Despretz, D. Stanicki, J. Rubio-Magnieto, M. Fossépré, M. Surin, S. Rorive, I. Salmon, L. Vander Elst, S. Laurent, R.N. Muller, S. Saussez, C. Burtea, Toward a new and noninvasive diagnostic method of papillary thyroid cancer by using peptide vectorized contrast agents targeted to galectin-1, Med. Oncol. 34 (11) (2017) 184, https://doi.org/10.1007/s12032-017-1042-y.

[30] S. André, L. Larbanoix, S. Verteneuil, D. Stanicki, D. Nonclercq, L. Vander Elst, S. Laurent, R.N. Muller, C. Burtea, Development of an LDL receptor-targeted peptide susceptible to facilitate the brain access of diagnostic or therapeutic agents, Biology (Basel) 9 (7) (2020) 161, https://doi.org/10.3390/biology9070161.

[31] C. Burtea, S. Laurent, T. Sanli, D. Fanfone, A. Devalckeneer, S. Sauvage, M.C. Beckers, S. Rorive, I. Salmon, L. Vander Elst, B.R. Lauwerys, R.N. Muller, Screening for peptides targeted to IL-7Rα for molecular imaging of rheumatoid arthritis synovium, Arthritis Res. Ther. 18 (1) (2016) 230, https://doi.org/10.1186/s13075-016-1133-8.

[32] C. Burtea, S. Ballet, S. Laurent, O. Rousseaux, A. Dencausse, W. Gonzalez, M. Port, C. Corot, L. Vander Elst, R.N. Muller, Development of a magnetic resonance imaging protocol for the characterization of atherosclerotic plaque by using vascular cell adhesion molecule-1 and apoptosis-targeted ultrasmall superparamagnetic iron oxide derivatives, Arterioscler. Thromb. Vasc. Biol. 32 (6) (2012) e36–48, https://doi.org/10.1161/ATVBAHA.112.245415.

[33] K.W. Dunn, M.M. Kamocka, J.H. McDonald, A practical guide to evaluating colocalization in biological microscopy, Am. J. Physiol. Cell Physiol. 300 (4) (2011) C723–C742, https://doi.org/10.1152/ajpcell.00462.2010.

[34] D. Fanfone, D. Stanicki, D. Nonclercq, M. Port, L. Vander Elst, S. Laurent, R.N. Muller, S. Saussez, C. Burtea, Molecular imaging of galectin-1 expression as a biomarker of papillary thyroid cancer by using peptide-functionalized imaging probes, Biology (Basel) 9 (3) (2020) 53, https://doi.org/10.3390/biology9030053.

[35] J. Rey, S. Murail, S. de Vries, P. Derreumaux, P. Tufféry, PEP-FOLD4: a pH-dependent force field for peptide structure prediction in aqueous solution, Nucleic Acids Res. 51 (W1) (2023) W432–W437, https://doi.org/10.1093/nar/gkad376.

[36] H. Ogiso, R. Ishitani, O. Nureki, S. Fukai, M. Yamanaka, J.H. Kim, K. Saito, A. Sakamoto, M. Inoue, M. Shirouzu, S. Yokoyama, Crystal structure of the complex of human epidermal growth factor and receptor extracellular domains, Cell 110 (6) (2002) 775–787, https://doi.org/10.1016/s0092-8674(02)00963-7.

[37] J.M. Sanders, M.E. Wampole, M.L. Thakur, E. Wickstrom, Molecular determinants of epidermal growth factor binding: a molecular dynamics study, PLoS One 8 (1) (2013) e54136, https://doi.org/10.1371/journal.pone.0054136.

[38] P. Zhou, B. Jin, H. Li, S.Y. Huang, HPEPDOCK: a web server for blind peptide–protein docking based on a hierarchical algorithm, Nucleic Acids Res. 46 (W1) (2018) W443–W450, https://doi.org/10.1093/nar/gky357.

[39] M. Ragazzi, A. Ciarrocchi, V. Sancisi, G. Gandolfi, A. Bisagni, S. Piana, Update on anaplastic thyroid carcinoma: morphological, molecular, and genetic features of the most aggressive thyroid cancer, Int. J. Endocrinol. 2014 (2014) 790834, https://doi.org/10.1155/2014/790834.

[40] M.M. Moasser, The oncogene HER2: its signaling and transforming functions and its role in human cancer pathogenesis, Oncogene 26 (45) (2007) 6469–6487, https://doi.org/10.1038/sj.onc.1210477.

[41] W. Wei, D. Jiang, Z.T. Rosenkrans, T.E. Barnhart, J.W. Engle, Q. Luo, W. Cai, HER2-targeted multimodal imaging of anaplastic thyroid cancer, Am. J. Cancer Res. 9 (11) (2019) 2413–2427.

[42] S. Sigismund, D. Avanzato, L. Lanzetti, Emerging functions of the EGFR in cancer, Mol. Oncol. 12 (1) (2018) 3–20, https://doi.org/10.1002/1878-0261.12155.

[43] G. Caldieri, M.G. Malabarba, P.P. Di Fiore, S. Sigismund, EGFR trafficking in physiology and cancer, Prog. Mol. Subcell. Biol. 57 (2018) 235–272, https://doi.org/10.1007/978-3-319-96704-2_9.

[44] S. Revathidevi, A. Kannan Munirajan, Akt in cancer: mediator and more, Semin. Cancer Biol. 59 (2019) 80–91, https://doi.org/10.1016/j.semcancer.2019.06.002.

[45] N.L.C. Bui, V. Pandey, T. Zhu, L. Ma, P.E. Lobie, Bad phosphorylation as target of inhibition in oncology, Cancer Lett. 415 (2018) 177–186, https://doi.org/10.1016/j.canlet.2017.11.017.

[46] C. Burtea, S. Laurent, E. Lancelot, S. Ballet, O. Murariu, O. Rousseaux, M. Port, L. Vander Elst, C. Corot, R.N. Muller, Peptidic targeting of phosphatidylserine for the MRI detection of apoptosis in atherosclerotic plaques, Mol. Pharm. 6 (6) (2009) 1903–1919, https://doi.org/10.1021/mp900106m.

[47] D. Crombez, S. Delcambre, D. Nonclercq, L. Vander Elst, S. Laurent, M. Cnop, R. N. Muller, C. Burtea, Modulation of adiponectin receptors AdipoR1 and AdipoR2 by phage display-derived peptides in in vitro and in vivo models, J. Drug Target. 28 (7–8) (2020) 831–851, https://doi.org/10.1080/1061186X.2019.1710840.

[48] C. Coman, E. Vlase, A. Dinu, Hematological and plasma biochemical values in four specific pathogen-free mice strains produced in the animal facility at Cantacuzino Institute, Bucharest, Sci. Works Ser. C Vet. Med. LXIV (1) (2018).

[49] Y. Zhu, X. Xiao, G. Li, J. Bu, W. Zhou, S. Zhou, Isoflurane anesthesia induces liver injury by regulating the expression of insulin-like growth factor 1, Exp. Ther. Med. 13 (4) (2017) 1608–1613, https://doi.org/10.3892/etm.2017.4157.

[50] S.T. Lee, T.T. Wu, P.Y. Yu, R.M. Chen, Apoptotic insults to human HepG2 cells induced by S-(+)-ketamine occurs through activation of a Bax–mitochondria–caspase protease pathway, Br. J. Anaesth. 102 (1) (2009) 80–89, https://doi.org/10.1093/bja/aen322.

[51] C. Burtea, S. Laurent, T. Sanli, D. Fanfone, A. Devalckeneer, S. Sauvage, M.C. Beckers, S. Rorive, I. Salmon, L. Vander Elst, B.R. Lauwerys, R.N. Muller, Screening for peptides targeted to IL-7Rα for molecular imaging of rheumatoid arthritis synovium, Arthritis Res. Ther. 18 (1) (2016) 230, https://doi.org/10.1186/s13075-016-1133-8.

[52] D. Chen, T.X. Tang, H. Deng, X.P. Yang, Z.H. Tang, Interleukin-7 biology and its effects on immune cells: mediator of generation, differentiation, survival, and

homeostasis, Front. Immunol. 12 (2021) 747324, https://doi.org/10.3389/fimmu.2021.747324.
[53] C.M. Li, P. Haratipour, R.G. Lingeman, J.J.P. Perry, L. Gu, R.J. Hickey, L.H. Malkas, Novel peptide therapeutic approaches for cancer treatment, Cells 10 (11) (2021) 2908, https://doi.org/10.3390/cells10112908.
[54] B. Todaro, E. Ottalagana, S. Luin, M. Santi, Targeting peptides: the new generation of targeted drug delivery systems, Pharmaceutics 15 (6) (2023) 1648, https://doi.org/10.3390/pharmaceutics15061648.
[55] I. Landa, T. Ibrahimpasic, L. Boucai, R. Sinha, J.A. Knauf, R.H. Shah, S. Dogan, J. C. Ricarte-Filho, G.P. Krishnamoorthy, B. Xu, N. Schultz, M.F. Berger, C. Sander, B. S. Taylor, R. Ghossein, I. Ganly, J.A. Fagin, Genomic and transcriptomic hallmarks of poorly differentiated and anaplastic thyroid cancers, J. Clin. Invest. 126 (3) (2016) 1052–1066, https://doi.org/10.1172/JCI85271.
[56] N. Pozdeyev, L.M. Gay, E.S. Sokol, R. Hartmaier, K.E. Deaver, S. Davis, J.D. French, P.V. Borre, D.V. LaBarbera, A.C. Tan, R.E. Schweppe, L. Fishbein, J.S. Ross, B. R. Haugen, D.W. Bowles, Genetic analysis of 779 advanced differentiated and anaplastic thyroid cancers, Clin. Cancer Res. 24 (13) (2018) 3059–3068, https://doi.org/10.1158/1078-0432.CCR-18-0373.
[57] K.C. Bible, E. Kebebew, J. Brierley, J.P. Brito, M.E. Cabanillas, T.J. Clark Jr, A. Di Cristofano, R. Foote, T. Giordano, J. Kasperbauer, K. Newbold, Y.E. Nikiforov, G. Randolph, M.S. Rosenthal, A.M. Sawka, M. Shah, A. Shaha, R. Smallridge, C.K. Wong-Clark, 2021 American Thyroid Association guidelines for management of patients with anaplastic thyroid cancer, Thyroid 31 (3) (2021) 337–386, https://doi.org/10.1089/thy.2020.0944. Erratum in: Thyroid 31 (10) (2021) 1606–1607, https://doi.org/10.1089/thy.2020.0944.correx.
[58] M.E. Cabanillas, M. Ryder, C. Jimenez, Targeted therapy for advanced thyroid cancer: kinase inhibitors and beyond, Endocr. Rev. 40 (6) (2019) 1573–1604, https://doi.org/10.1210/er.2019-00007.
[59] S. Saini, K. Tulla, A.V. Maker, K.D. Burman, B.S. Prabhakar, Therapeutic advances in anaplastic thyroid cancer: a current perspective, Mol. Cancer 17 (1) (2018) 154, https://doi.org/10.1186/s12943-018-0903-0.
[60] X. Gao, C. Hong, Y. Xie, X. Zeng, Immunotherapy or targeted therapy: what will be the future treatment for anaplastic thyroid carcinoma? Front. Oncol. 13 (2023) 1103147 https://doi.org/10.3389/fonc.2023.1103147.
[61] M.H. Ge, X.H. Zhu, Y.M. Shao, C. Wang, P. Huang, Y. Wang, Y. Jiang, Y. Maimaitiyiming, E. Chen, C. Yang, H. Naranmandura, Synthesis and characterization of CD133 targeted aptamer-drug conjugates for precision therapy of anaplastic thyroid cancer, Biomater. Sci. 9 (4) (2021) 1313–1324, https://doi.org/10.1039/d0bm01832e.